Nano Research

Open Access

Review Article

Emerging techniques for environmental nanoplastic pollutants detecting

Jilun Wang, Minglu Ma, Licheng Wang, Yajuan Yu, and Liwu Zhang ✉

Shanghai Key Laboratory of Air Quality and Environmental Health, Department of Environmental Science and Engineering, Fudan University, Shanghai 200433, China

Cite this article: *Nano Research*, **2026**, *19*, 94908506. https://doi.org/10.26599/NR.2026.94908506

ABSTRACT: Microplastics (MPs, < 5 mm) and nanoplastics (NPs, < 1 μm) have emerged as pervasive environmental contaminants due to the extensive use and continuous release of plastic materials. Despite growing awareness of their ecological and health risks, achieving rapid, accurate, and multidimensional detection of these particles remains a formidable analytical challenge. This review identifies the major analytical challenges in detecting NPs within environmental matrices and synthesizes recent advances across mass spectrometry, spectroscopy, and optical/electron microscopy, supported by machine learning and microfluidics. These emerging techniques enable faster, more accurate detection of smaller NPs and improve discrimination among polymer types and coexisting materials. We introduce a functionality and performance-oriented framework that classifies detection strategies into four capability domains reflecting future requirements: (1) high-throughput quantification of particle concentration, (2) accurate polymer identification, (3) spatially resolved imaging of particle distributions, and (4) *in situ* multimodal analysis. By transcending traditional instrument-based classifications, this framework enables meaningful cross-method comparisons under shared analytical objectives and underscores a broader transition in the field toward multimodal integration, advanced data analytics, and *in situ* characterization. We synthesize the strengths of emerging analytical strategies, propose quantitative performance benchmarks, and provide guidance for their effective translation into real-world environmental monitoring.

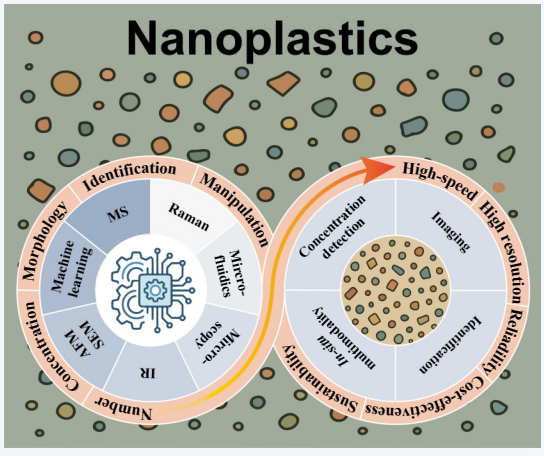

KEYWORDS: nanoplastics, rapid detection, quantitative, identification, imaging

1 Introduction

Driven by the pervasive use of plastic materials and their continual release into natural systems, microplastics (MPs, < 5 mm) and nanoplastics (NPs, < 1 μm)—collectively termed MNPs—have become contaminants of growing global concern. Attributable to their chemical inertness and minute dimensions, MNPs exhibit exceptional environmental persistence and mobility, leading to their ubiquitous distribution across diverse matrices, including the atmosphere [1–4], aquatic systems [5–9], soils [10], sediments [11], solid wastes [12], and even remote ecosystems such as the polar regions [13] and high mountains [14, 15]. With their high specific surface area and strong hydrophobicity, MNPs serve as vectors for organic pollutants [16, 17], heavy metals [18], and antibiotic resistance genes [19], forming complex pollutant composites. Furthermore, as plastics undergo photochemical, mechanical, chemical, and biological aging, their physicochemical properties undergo dynamic transformations. These changes modulate the ecotoxicological effects of MNPs, resulting in increasingly complex environmental behaviors and elevated health risks [20].

The threat of MNPs to ecological safety and human health manifests through dual pathways. On one hand, MNPs can be ingested by organisms across multiple trophic levels, exerting direct toxicological effects [21–31]. On the other hand, acting as a unique plastisphere niche [32, 33], MNPs can selectively enrich specific bacterial communities and drive the dissemination of antibiotic resistance genes (ARGs) [34], constituting an insidious yet profound indirect biological hazard.

Concerning the direct exposure risks, NPs exhibit significantly

Received: December 2, 2025; **Revised:** January 21, 2026
Accepted: January 29, 2026

✉Address correspondence to zhanglw@fudan.edu.cn

higher potential toxicity than MPs. This is primarily attributed to their nanoscale dimensions approaching the pore size of biological membranes, endowing them with penetration characteristics similar to engineered nanomaterials in tumor microenvironments [35]. This distinct size effect enables NPs to easily traverse biological barriers, accumulate in intracellular compartments, and induce DNA damage via reactive oxygen species (ROS)-mediated oxidative stress pathways [21]. Mechanistically, NPs disrupt gut barrier integrity by downregulating the expression of tight junction proteins, triggering the release of pro-inflammatory cytokines and gut dysbiosis [36]. This persistent inflammatory microenvironment further perturbs the homeostasis of activating and inhibitory receptors on natural killer (NK) cells, inducing functional exhaustion and impairing immune surveillance capabilities [37]. As host immune defenses are compromised, commensal microbes may transform into opportunistic pathogens, disrupting host health homeostasis [38]. These cascade reactions collectively foster a microenvironment conducive to tumor immune escape and proliferation. Furthermore, acting as a "trojan horse", NPs adsorb environmental toxins (e.g., bisphenol A) and pathogens, creating synergistic cytotoxicity that further activates carcinogenic signaling pathways [36]. Consequently, the precise identification and quantification of NPs within complex environmental and biological matrices are indispensable prerequisites for deciphering their environmental fate and toxicological mechanisms. Driven by this imperative, the research frontier is rapidly expanding from NPs to the biologically more potent yet analytically elusive NPs.

Extensive research efforts regarding NP detection have spurred a plethora of reviews summarizing the analytical landscape. These reviews generally fall into two primary frameworks. The first comprises method-oriented reviews, which comprehensively evaluate approaches such as Fourier-transform infrared spectroscopy (FTIR), Raman spectroscopy (Raman) [39–46], mass spectrometry (MS) [47], electrochemical sensing, and thermal analysis. These discussions emphasize analytical performance, detection limits, and applicability [48–53], with machine learning increasingly highlighted as a pivotal tool for data enhancement [54, 55]. The second category includes environment-oriented reviews, which examine detection strategies and contamination characteristics across diverse environmental matrices, including water, soil, air, and sediments [1–12, 21, 23, 24, 40, 56]. Early studies laid a solid methodological foundation for NPs analysis, primarily addressing the fundamental question of detection feasibility. With continued advancements, the research focus has evolved toward strategies for achieving faster, more accurate, and multidimensional detection. Recent breakthroughs increasingly rely on the synergistic integration of multidisciplinary approaches, multifunctional platform designs, and multimodal characterization. Drawing upon principles from optics, electrochemistry, materials science, and precision instrumentation, these developments mark a paradigm shift in NPs analysis—from conventional environmental science toward a more comprehensive, interdisciplinary framework. Given this diversification, categorizing detection methods solely by analytical principles no longer suffices to capture their performance nuances or practical relevance, nor does it facilitate effective comparison. Accordingly, future research should be driven by real-world detection needs and adopt a problem-oriented perspective to establish more targeted, comparable, and application-oriented detection strategies.

To address the expanding complexity of NP detection, this review proposes a functionality-driven classification framework. The manuscript is organized as follows: Section 2 identifies critical bottlenecks hindering current detection efforts. Section 3 categorizes emerging strategies into four performance-oriented domains: (i) rapid quantification, prioritizing high-throughput and cost-effective workflows; (ii) polymer identification, focusing on minimized pretreatment and expedited analysis; (iii) spatial imaging, highlighting high-resolution visualization in complex matrices; (iv) multimodal integration, enabling comprehensive *in situ* characterization. Section 4 synthesizes the current research landscape and introduces the R^{3}ES framework—a disclosure protocol designed to benchmark the operational performance of detection methods. This initiative aims to accelerate the translation of NPs detection from exploratory research to standardized, real-world applications.

2 The dilemma of NPs detection

The detection of NPs constitutes a formidable analytical challenge, driven by their intrinsic colloidal heterogeneity and trace-level occurrence in complex environmental matrices. The critical bottlenecks manifest across four dimensions:

1) **Methodological incompatibility in pre-treatment:** Sample pretreatment is undeniably critical for reliable detection, yet conventional protocols designed for NPs often hit a wall at the nanoscale. The first major hurdle is chemical stability. Aggressive digestion methods, while effective for larger plastics, can inflict irreversible damage on NPs [57, 58]. This degradation has a dual negative impact: It reduces recovery rates, leading to underestimation in mass-based quantification via pyrolysis-gas chromatography/mass spectrometry (Py-GC/MS) [59–62]. Consistent with the findings of Shi et al. [61], measured nanoplastic concentrations were generally lower using the filtration-based Py-GC/MS method compared to direct spectroscopic enrichment. Taking river water as a representative example, the Py-GC/MS method detected 5.6±0.6 μg·L^{-1}, significantly lower than the 6.5–8.5 μg·L^{-1} range obtained spectroscopically. It also distorts spectral fidelity, and in techniques like Raman and FTIR, surface oxidation often introduces misleading carbonyl peaks that mask the polymer's true fingerprint [59]. Second, separation strategies relying on size exclusion and density flotation frequently fail. NPs exhibit a high propensity for membrane fouling (pore blocking) during filtration or irreversible aggregation during enrichment [59]. Such phenomena result in significant analyte loss, leading to underestimation in mass spectrometry and inducing artifacts in light-scattering assays like dynamic light scattering (DLS) and nanoparticle tracking analysis (NTA). It can reduce particle counts and pseudo-shifts in size distribution. Finally, environmental NPs spontaneously adsorb biomolecules or humic substances to form an eco-corona [63]. This coating significantly alters surface hydrophobicity and effective density [64–66], thereby rendering density-based flotation separation ineffective.

To navigate these hurdles, recent research has shifted toward refining pretreatment architectures. Crucially, mild digestion strategies utilizing hydrogen peroxide (H_2O_2) and enzymes have been introduced to preserve the physicochemical integrity of NPs, avoiding the destructive effects of harsh acids or alkali [57]. On the separation front, asymmetric-flow field-flow fractionation (AF4) offers a compelling alternative to traditional filtration. By leveraging cross-flow fields within a semi-permeable channel rather than

forcing particles through pores, AF4 effectively mitigates the membrane clogging issues that plague conventional methods [59]. In parallel, two-stage density separation protocols have been optimized to heighten selectivity in complex matrices. To further minimize aggregation, ultrasonic dispersion in anhydrous ethanol is utilized to sever van der Waals forces between particles, whereas gentle nitrogen blow-drying offers a non-thermal alternative to solvent removal, thereby circumventing heat-induced agglomeration [59]. It is worth noting that these methods are rarely one-size-fits-all; they typically necessitate rigorous tailoring aligned with the specific polymer identities of the target NPs.

2) **The sensitivity-throughput paradox:** A persistent trade-off exists between detection sensitivity and analytical throughput. Optical techniques are fundamentally constrained by the diffraction limit. This physical barrier restricts spatial resolution, severely impeding the detection of small-sized NPs via micro-Raman and micro-FTIR. Conversely, techniques that offer high resolution, such as traditional electron microscopy (EM), are hampered by a notoriously narrow field of view, making large-scale scanning impractical. Mass spectrometry presents a different challenge: While chemically specific, it is bottlenecked by laborious sample introduction protocols, rendering rapid, high-throughput screening largely unfeasible. Therefore, new methods need to be developed. Addressing this critical need constitutes the primary motivation of this work.

3) **Stochasticity in data analysis:** Extracting weak signals from high-noise environmental backgrounds remains labor-intensive and error-prone. Furthermore, the integration of artificial intelligence (AI) for spectral deconvolution is in its nascent stage, lacking a systematic, data-driven framework for automated and robust particle recognition. This necessitates collaborative efforts from the academic community to share relevant data, facilitating the training of more robust and accurate models.

4) **Quantification bias via standardization gaps:** Current research relies disproportionately on pristine, spherical commercial microspheres, ignoring the morphological and chemical complexity of weathered NPs (e.g., irregularity, oxidation, and fragmentation). Consequently, quantification models derived from light scattering or mass spectrometry are prone to substantial systematic bias when extrapolated to real-world samples. This step requires further collective efforts from the research community to advance.

3 Emerging technologies for NPs detection

3.1 Rapid concentration detection

The quantification of environmental NPs typically relies on two distinct metrics: mass concentration and number concentration. Mass concentration is currently the primary metric, typically determined via Py-GC/MS. Expressed in units such as $\mu g \cdot L^{-1}$ or $mg \cdot kg^{-1}$, it aligns with established protocols for bulk pollutants. Conversely, number concentration, represents the particle density per unit volume (e.g., $particles \cdot L^{-1}$), emphasizing particle-level exposure frequency and biological interactions. This metric is pivotal for elucidating microscopic toxicological mechanisms and transport dynamics [67]. These two concentration metrics are mathematically interconvertible because the mass of a particle is proportional to the cube of its aerodynamic diameter. Specifically, the total mass concentration is derived by integrating the product of the single-particle mass and the distribution function of particle number. This conversion typically relies on the assumption that particle sizes follow a log-normal distribution. Due to the cubic relationship between particle diameter and volume, a reduction in size triggers an exponential surge in number concentration at a constant mass. A case in point is the atmospheric study in Shanghai, where NP number concentrations exceeded those of NPs by over three orders of magnitude (~ 3,055-fold) [68]. Furthermore, the drastically increased specific surface area of NPs emerges as a critical third dimension—complementary to mass and number—for elucidating environmental fate and biological interactions [69]. Accurate quantification of this parameter necessitates a comprehensive integration of particle size distribution and number concentration characteristics. Looking ahead, a framework combining mass and number concentrations holds promise for establishing a unified exposure metric and risk grading system, thereby providing a robust scientific foundation for standardized environmental monitoring and interdisciplinary risk assessment of NPs.

3.1.1 *Rapid quantification of number concentration*

Optical and electron microscopy are commonly used for particle quantification, yet the diffraction limit of light severely restricts optical microscopy from detecting NPs. To overcome this, Ludescher et al. [70] developed an optical sieve that used Mie void resonances capable of identifying NPs as small as 200 nm using an optical microscope with an RGB (RGB = red, green, and blue) sensor camera. The Mie voids are fabricated via electron-beam lithography combined with dry etching in gallium arsenide (GaAs). This approach markedly simplifies the workflow and reduces production time, enabling cost-effective, disposable test strips. Functionally, Mie voids trap NPs matching their cavity size. Particle presence, size, and distribution can be inferred from cavity color changes. Distinct color shifts corresponding to particle number or size (e.g., blue or red) enable precise quantification via a standardized color reference (Figs. 1(a)–1(d)). This method efficiently processes environmental samples by selectively retaining NPs that match cavity sizes while removing impurities, greatly simplifying detection and reducing analysis time. Furthermore, integration with FTIR or Raman spectroscopy further enables detailed material characterization, offering a powerful tool for NPs analysis in complex environmental and biological matrices.

Inductively coupled plasma mass spectrometry (ICP-MS) in single-particle mode (SP-ICP-MS) can also be employed for rapid counting and size analysis of NPs. The core principle of SP-ICP-MS is that each detected event corresponds to a single particle, requiring highly diluted suspensions ($< \sim 10^8$ $particles \cdot L^{-1}$) and high acquisition frequencies (> 100 Hz). Under these conditions, event intensity is proportional to the element mass per particle, enabling particle size determination when composition, shape, and density are known [71]. Particle number concentration is derived from the frequency of recorded events and the transport efficiency, while event intensity allows estimation of element mass and size distributions for solid, spherical, and pure particles. Metal functionalization of NPs plays a crucial role, with palladium [72] and gold [73] showing superior probes performance. Most studies still rely on lab-synthesized spherical NPs, mainly polystyrene (PS), though research on irregular or fibrous NPs is increasing [47]. Researchers further demonstrated that monitoring ^{13}C enabled quantitative determination of NPs size and abundance without metal doping or complex sample pretreatment [74]. Liu et al. [75]

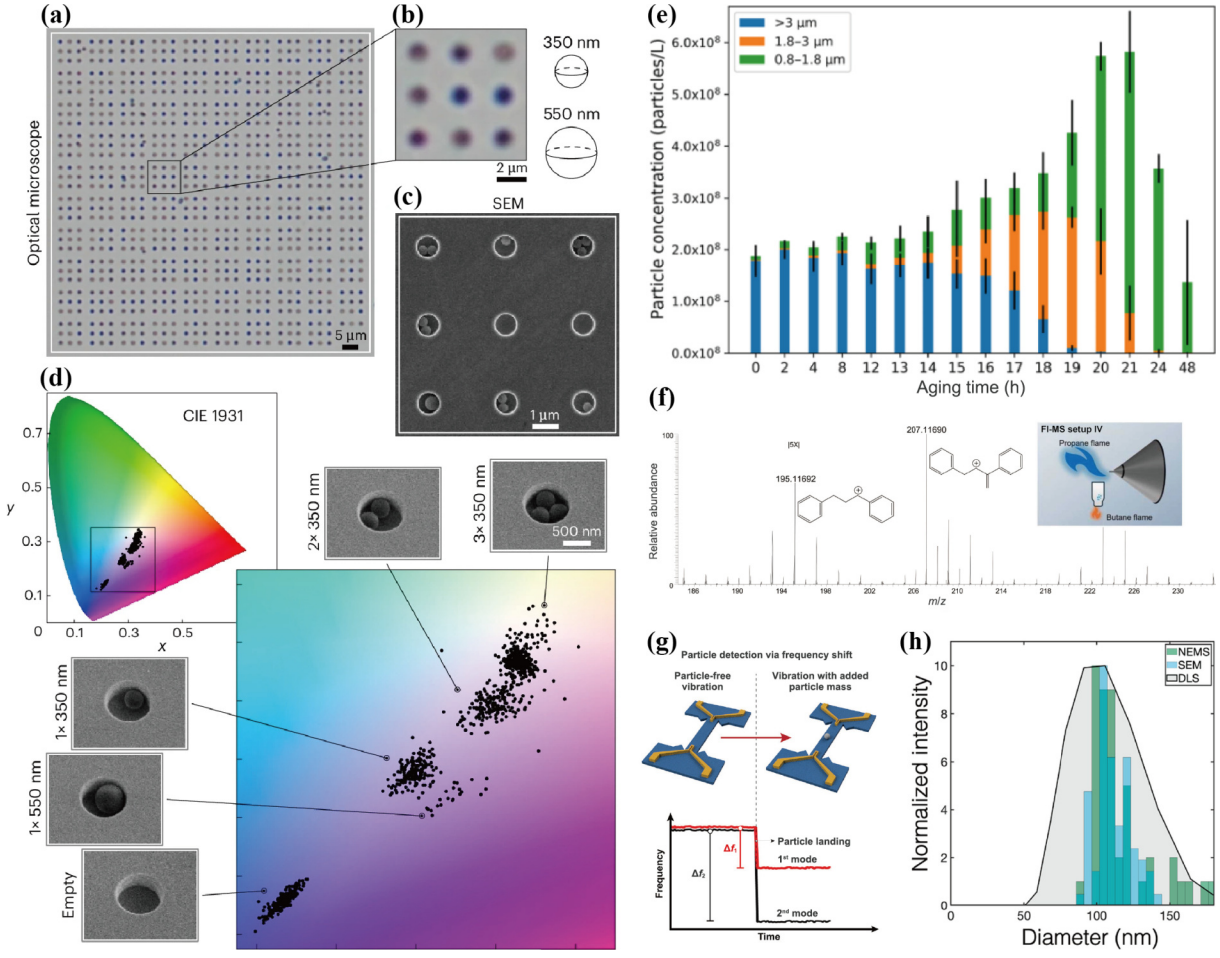

Figure 1 Strategies for rapid detection of number concentration and mass concentration. (a) Optical microscopy and (b) the corresponding magnified region reveal five distinct color states arising from different void-occupation configurations, achieved by depositing 350 and 550 nm spherical NPs onto the substrate. (c) Scanning electron microscopy (SEM) image of the magnified region confirms the presence of all five states within the 3 × 3 array: an empty void; voids occupied by one, two, or three 350 nm spheres; and a void containing a single 550 nm sphere. (d) Colorimetric analysis of the full optical image is plotted in the CIE 1931 chromaticity diagram. The inset highlights the separation of the five color states, and representative SEM images of each occupied state are displayed around the diagram for reference. Reproduced with permission from Ref. [70], © Ludescher et al. 2025. (e) Particle number concentration of PS during the aging process as determined by SP-ICP-MS. Reproduced with permission from Ref. [75], © American Chemical Society 2021. (f) FI-MS spectrum of standard 100 nm PS NPs. Reproduced with permission from Ref. [86], © Elsevier B.V. 2025. (g) Principle of NEMS detection: incoming particles or virions are subsequently detected by a NEMS resonator operating simultaneously in its first two out-of-plane flexural modes, enabling determination of both the mass and landing position of each particle. (h) Comparison of NEMS-MS, SEM, and DLS diameter measurements for 100 nm PS. In each panel, the *y*-axis represents particle counts for NEMS-MS and SEM, and normalized scattering intensity for DLS. Reproduced with permission from Ref. [87], © American Chemical Society 2022.

showed that ^{13}C-based SP-ICP-MS can precisely count 800 nm–5 μm PS particles (Fig. 1(e)) and revealed that photodegradation generated numerous smaller MNPs. Gonzalez de Vega et al. [76] improved size detection limits to 620 nm in ultrapure water and 960 nm in seawater using ^{12}C. Hendriks et al. [77] successfully counted NPs in high-dissolved organic carbon (DOC) matrices and distinguished them from other carbonaceous particles. Despite advances in ICP-MS enabling real-sample detection, investigations into the actual environmental presence of NPs remain scarce.

3.1.2 *Rapid quantification of mass concentration*

Py-GC/MS is a widely used technique for NPs detection, enabling precise polymer identification and reliable mass-based quantification in complex matrices [78–80]. The technique operates by thermally decomposing polymer samples into characteristic monomeric or fragment molecules, which are subsequently separated via gas chromatography and identified by mass spectrometry. However, despite its chemical specificity, the application of mass spectrometry to NPs is hindered by three fundamental limitations: (1) the intrinsic loss of morphological information (e.g., size, shape, and particle count) due to the destructive nature of thermal decomposition; (2) sample loss and compromised reproducibility stemming from labor-intensive pre-treatment steps, such as nitric acid digestion, density separation, and multi-step extraction; (3) false positives arising from natural organic matter (NOM) producing pyrolysis products indistinguishable from target polymers. To mitigate these limitations, thermal extraction desorption-gas chromatography/mass spectrometry (TED-GC/MS) circumvents analyte attenuation associated with laborious pretreatment via direct solid sampling. Concurrently [81, 82], tandem mass spectrometry (MS/MS) [83] and high-resolution mass spectrometry (HRMS) [84, 85] leverage superior spectral resolution to effectively resolve matrix interferences. Additionally, single particle inductively coupled

plasma mass spectrometry (SP-ICP-MS) [73, 74, 77] partially addresses the deficit in physical characterization (size and count) for specific particle classes. Nevertheless, a fundamental void persists regarding the non-destructive mass measurement and high-efficiency ionization of pristine carbonaceous NPs. This challenge has catalyzed the emergence of innovative principles—specifically flame ionization mass spectrometry (FI-MS) and nanoelectromechanical systems-based mass spectrometry (NEMS-MS). These innovations offer transformative solutions to transcend these enduring detection bottlenecks.

Flame ionization mass spectrometry (FI-MS). FI-MS uses a flame as the ionization source to thermally decompose and ionize organic compounds, with the resulting ions analyzed by mass spectrometry according to their mass-to-charge ratio (m/z). Combining high ionization efficiency with strong selectivity, FI-MS enables rapid and sensitive detection of organic particulates. Xiao et al. [86] developed FI-MS for rapid, direct, and sensitive detection of NPs, achieving a minimum detectable particle size of 100 nm (Fig. 1(f)). Plastic samples are combusted in a high-temperature flame, producing characteristic ions, allowing single analyses in ~ 10 s with minimal pretreatment. This strategy can directly analyze plastics in water, juice, soil, and biological tissues (e.g., mouse placenta) without extraction or digestion, simplifying workflows and reducing sample loss. Although its polyethylene terephthalate (PET) detection limit (0.25 μg) is higher than that of Py-GC/MS (0.02 μg), FI-MS offers clear advantages for rapid screening and quantification.

NEMS-MS. NEMS-MS is an emerging MS technique that measures the mass of individual particles or molecules by monitoring the resonance frequency shifts of nanoscale mechanical resonators, enabling non-ionizing and non-destructive mass detection. Erdogan et al. [87] demonstrated atmospheric-pressure NEMS-MS for detecting 100 nm NPs. By integrating a NEMS sensor with a polymer lens on a single chip, the system enables single-particle mass measurements under ambient conditions, enhancing portability and simplifying instrumentation. Briefly, charged droplets containing NPs or virions are generated via electrospray ionization (ESI). As they evaporate, Rayleigh fission produces single particles that are directed toward the NEMS chip, which consists of an active resonator and a photoresist layer with an aligned aperture. The photoresist layer accumulates charge from incoming ions, electrostatically focusing them through the aperture onto the NEMS active area for mass detection (Figs. 1(g) and 1(h)). Incoming particles or virions are detected by a NEMS resonator operating in its first two flexural out-of-plane modes, enabling simultaneous determination of each particle's mass and impact position (Fig. 1(g)). The lens improves particle capture efficiency, reducing analysis time to under 30 min. With ~ 3.2 MDa mass resolution, the system distinguishes particles in the hundreds of MDa range, including 100 nm PS NPs (Fig. 1(h)). However, chemical composition cannot be identified, necessitating complementary analytical techniques.

3.2 Rapid identification of particle types

Surface-enhanced Raman spectroscopy (SERS) provides a highly sensitive, non-destructive, rapid approach for analyzing NPs by leveraging their characteristic molecular "fingerprint" peaks, while also enabling *in situ* detection. As a result, SERS has become an essential analytical technique in NPs research. Several comprehensive reviews have summarized the principles, substrate fabrication methods, and applications of SERS in NPs detection [41, 43, 46]. Despite these advances, practical implementation remains challenged by complex sample preparation, low throughput in large-area scanning, limited spatial resolution, and poor substrate reproducibility. Recent progress in nanostructure-based substrates, multimodal SERS strategies, and multifunctional sensor designs has markedly improved sensitivity, resolution, and reusability. This chapter highlights recent SERS developments with a focus on performance optimization, material design, and multifunctional integration.

3.2.1 *Strategies for detecting nanoscale single-particle*

High-performance SERS techniques are crucial for NPs detection, ideally enabling the acquisition of signals from individual particles at the smallest possible size, thereby maximizing sensitivity and spatial resolution. Achieving single-particle detection of NPs requires substrates with signal-enhancing nanostructures and robust data processing to ensure accuracy. These substrates commonly possess well-ordered nanoscale architectures and hydrophilic surfaces (Fig. 2(a)) to obtain relatively uniform SERS hotspots and to prevent nanoparticle aggregation, in contrast to hydrophobic surface-based enrichment strategies discussed later. In a representative study, Wu et al. [88] developed a reusable hydrophilic anodic aluminum oxide (AAO) membrane sensor integrated with a Raman data-processing algorithm (Pre_seg) for simultaneous imaging, chemical identification, and quantification of PS and PE (300–500 nm) in real lake water. Acting as both a filtration substrate and a Raman sensor, the AAO membrane enabled quantitative detection at 0.1 s per pixel while reducing sample loss, contamination, and cost (Fig. 2(b)). The Pre_seg algorithm optimized signal-to-noise ratio (SNR) and full width at half maximum (FWHM) thresholds to suppress noise, achieving 93.5% nanoparticle detection accuracy and ≥ 90.4% exclusion of non-nanoplastic signals (Figs. 2(c) and 2(d)). This method surpasses conventional Raman microscopy, providing a low-cost, high-reproducibility platform capable of detecting environmentally relevant concentrations. Complementing such membrane-based approaches, geometric optimization of substrates also plays a vital role. Liu et al. [89] developed Ag nanoarrays (AgNAs) with different inter-column spacings and heights and found that the signal intensity was maximized when inter-column spacing and height matched the particle size. Specifically, the strongest enhancement occurred for 180 nm PS on AgNAs with 180 nm spacing and 180 nm height. Smaller gaps between PS NPs and the silver array edges produced stronger electromagnetic field enhancement, leading to increased SERS intensity. This structural-matching strategy enabled single and mixed detection of 500 nm PET, 500 nm polyethylene (PE), 1 μm polypropylene (PP), 1 μm polyvinyl chloride (PVC), and 130 nm PS with a limit of detection (LOD) of 10 μg·mL^{-1} and detected 130 nm PS in real water samples. Similarly, Zhang et al. [90] developed a low-cost, high-throughput gold triangular cavity array (TCA) substrate (Fig. 2(e)) capable of detecting 50 nm PS in water and PET (average 88.2 nm) from commercial bottled mineral water (Fig. 2(f)), achieving a LOD of 0.001% (1.5×10^{11} particles·mL^{-1}) for PS. Additionally, Lu et al. [91] established a paper-based portable SERS platform that successfully identified PS particles with diameters of 1010, 142, and 20 nm, as well as 610 nm nylon particles. For 20 nm PS, the platform achieved an enhancement factor (EF) of 10^{10} and LOD of 1 ppt, reaching single-particle sensitivity with minimal interference from

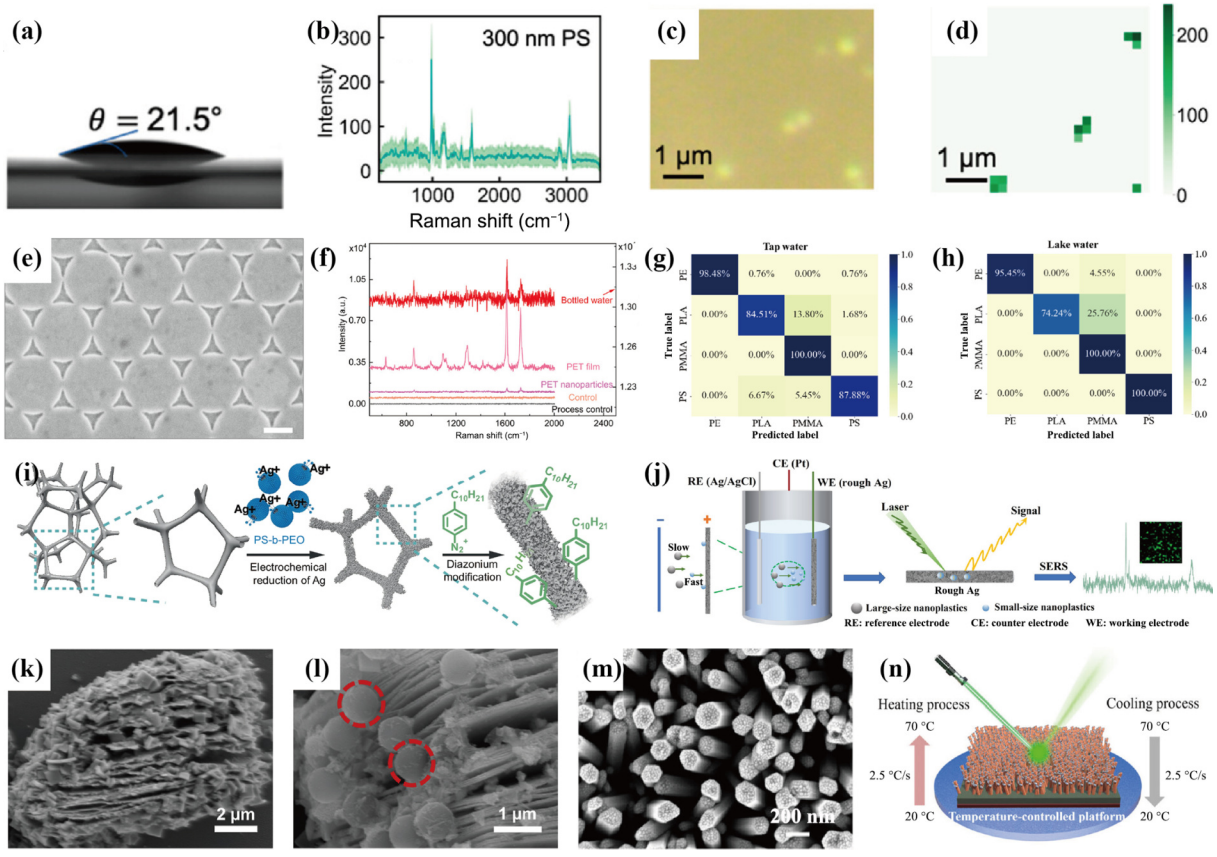

Figure 2 Strategies for nanoscale single-particle detection, accurate particle classification, and low-cost semiconductor-based SERS substrates. (a) Contact angle measurement of a deionized water droplet on a pristine AAO membrane (pore size = 20 nm). (b) Raman spectra of 300 nm PS deposited on 20 nm AAO membranes, obtained from 50 individual particles and averaged (dark green line); the light green shading indicates one standard deviation. (c) Dark-field optical images of 300 nm PS on 20 nm AAO membranes. (d) Raman mapping of 300 nm PS processed using Pre_seg. Reproduced with permission from Ref. [88], © American Chemical Society 2025. (e) SEM of gold triangular cavity array. (f) Raman spectra of the samples extracted from bottled drinking water on the TCA substrate (red line), the plain glass substrate (brown line), and the PET film (purple line). Reproduced with permission from Ref. [90], © American Chemical Society 2022. (g) and (h) Confusion matrices illustrating the classification performance of the KNN model for distinguishing four NPs types (PS, PMMA, PE, and PLA) in tap water and lake water. Reproduced with permission from Ref. [93], © American Chemical Society 2024. (i) Schematic of the electrodeposition process producing AgF@AgM, where porous Ag foam is coated with mesoporous Ag and subsequently passivated with 4-decylbenzene diazonium tosylate to form hydrophobic AgF@AgM@C10 substrates. Reproduced with permission from Ref. [94], © Guselnikova et al. 2024. (j) Electrosorption-based preconcentration and SERS detection of NPs using the ES-SERS platform. CE, RE, and WE denote the counter, reference, and working electrodes, respectively. Reproduced with permission from Ref. [95], © American Chemical Society 2024. SEM images of (k) $Ti_3C_2T_x/TiO_2/W_{18}O_{49}$ and (l) PS microplastic particles on the $Ti_3C_2T_x/TiO_2/W_{18}O_{49}$ substrate. Reproduced with permission from Ref. [97], © Elsevier B.V. 2025. (m) SEM image of Ag nanoparticles/ZnO nanorods/GaN (AZG) heterostructure SERS substrate and (n) the schematic illustration of Raman detection under variable temperature. Reproduced with permission from Ref. [98], © American Chemical Society 2025.

fluorescent model dyes. Collectively, these high-performance SERS substrates provide a robust foundation for subsequent rapid and highly sensitive analysis of NPs.

3.2.2 *Strategies for accurate classification*

The small Raman scattering cross-section and compositional heterogeneity of environmental NPs, often complicated by overlapping or shifted spectral signatures, render manual identification prone to subjectivity and inefficiency—especially in high-throughput scenarios. The integration of SERS substrates with AI or machine learning (ML) enables automated spectral classification and latent feature extraction. This synergy facilitates rapid, objective analysis, substantially amplifying both the precision and throughput of NP detection.

Generally, the AI workflow for NP detection initiates with the acquisition of raw spectral data. This is followed by rigorous preprocessing, including baseline correction and smoothing to yield high-fidelity datasets with optimized SNR. Subsequently, feature extraction and dimensionality reduction are executed utilizing algorithms such as principal component analysis (PCA) or t-distributed stochastic neighbor embedding (t-SNE). These extracted features serve as inputs for training classifiers like random forest (RF). Finally, the model outputs are subjected to interpretability analysis via tools like SHapley Additive exPlanations (SHAP) values or confusion matrices, effectively translating algorithmic predictions into chemically significant conclusions [54, 55]. Specifically, Xie et al. [92] utilized the "peak extraction and retention" (PEER) algorithm for spectral denoising, augmented by baseline correction and first-derivative processing to mitigate background interference and deconvolute overlapping peaks. By consolidating predictions via a voting mechanism, the RF model achieved an accuracy of 98.8%, outperforming both support vector machines (SVM) and back propagation neural networks (BPNN) in sensitivity and specificity. The model also exhibited robust anti-interference capabilities, particularly in salt-laden matrices. Ultimately, the successful identification of PS and PVC in spiked rainwater, verified

through confusion matrices and feature visualization, validates the system's efficacy for precise NP detection within challenging, low-SNR environments.

Ye et al. [93] integrated SERS with machine learning, leveraging metal–phenolic networks (MPNs) assembled from tannic acid (TA) and Zr^{4+}, to drive the rapid aggregation, separation, and signal amplification of NPs across diverse types and sizes. Following spectral acquisition, the workflow employed spectral truncation to eliminate substrate interference, alongside data augmentation to enhance model robustness. Furthermore, data integrity was refined by coupling support vector classifier (SVC)-based feature selection with the isolation forest algorithm for efficient outlier rejection. On this foundation, K-nearest neighbors (KNNs) and RF models were selected, achieving high-precision classification (accuracy ~ 97%) of various polymers. Simultaneously, t-SNE visualization and SHAP analysis elucidated the models' decision-making mechanisms. Concurrently, a polynomial regression model facilitated precise quantification of variable-sized NPs (R^2 = 0.9745). Validated in authentic complex matrices like tap and lake water (Figs. 2(g) and 2(h)), this cost-effective protocol reduced total operation time to ~30 min, underscoring its potential for high-throughput NP detection in complex systems.

Furthermore, Guselnikova et al. [94] combined SERS with a deep learning model, SpecATNet. The substrate design exploited short-range ordered topologies to maximize light absorption and plasmonic coupling, thereby intensifying Raman signal generation. Concurrently, hydrophobic surface functionalization (designated as AgF@AgM@C10) ensured the selective capture and long-term stability of NPs (Fig. 2(i)). Within the computational pipeline, massive raw spectral datasets underwent rigorous preprocessing (background subtraction and normalization) prior to deep feature encoding via a densely connected convolutional network (DenseNet) backbone. Crucially, a self-attention mechanism was embedded to dynamically weigh and accentuate key chemical fingerprints while suppressing noise from complex matrices, such as proteins and humic substances. Consequently, employing a multi-label classification strategy, the model achieved precise identification of low-concentration mixtures and their aging states in real-world samples. Notably, this workflow obviated the need for laborious pretreatment, marking a 20-fold efficiency gain over conventional Py-GC/MS.

Complementing these advancements in computational spectral analysis, physical separation strategies have also evolved to enable size-resolved detection. Wang et al. [95] introduced a hyphenated electrosorption and SERS (ES-SERS) method that enabled detection of NPs down to 30 ng·L^{-1}. A time-controlled electro-adsorption mechanism allowed selective enrichment of particles by size, as smaller PS migrated faster and generated stronger SERS signals on roughened silver surfaces (Fig. 2(j)). The method required only a weak potential to rapidly create dense "hotspots", reducing analysis time and eliminating complex pretreatment. Demonstrating strong resistance to interference from cations and organic dyes, ES-SERS was further validated for identifying and quantifying NPs leached from real-world samples such as beverage cup lids.

3.2.3 *Low-cost semiconductor SERS substrates*

Compared to conventional noble metal SERS substrates, semiconductor-based substrates are gaining attention for environmental monitoring and portable sensing applications due to their abundant material availability, simple fabrication process, and low cost. The enhancement of semiconductor is primarily due to chemical effects from the charge-transfer (CT) process between the semiconductor surface and absorbed molecules, which increases the polarizability (α) of the adsorbed targets, resulting in amplified Raman signals [96].

Han et al. developed a highly sensitive, uniform, and durable three-dimensional (3D) SERS sensor based on a $Ti_3C_2T_x/TiO_2/W_{18}O_{49}$ heterostructure, achieving precise 800 nm PS quantification in complex samples (rainwater, soil, industrial water) with a LOD of 25 μg·mL^{-1}, broad linear range, and excellent signal reproducibility [97]. The composite's narrow bandgap and high carrier mobility facilitate efficient electron–hole separation under laser excitation. The energy band difference between $Ti_3C_2T_x$ and TiO_2 drives hole migration, while plasmon resonance of $W_{18}O_{49}$ enhances electron transfer, generating both electromagnetic and chemical effects to amplify signals (Fig. 2(k)). PS becomes confined within the interlayer gaps, positioning it directly in intense SERS hotspots and enabling strong signal enhancement (Fig. 2(l)). After 500 bending cycles, the sensor retained 73% of its initial SERS intensity, demonstrating excellent mechanical stability. Expanding on heterostructure-based strategies, Dou et al. [98] employed a temperature-controlled platform with an Ag nanoparticle/ZnO nanorod/GaN heterostructure to introduce pyroelectric potential, significantly enhancing SERS performance. Densely distributed Ag nanoparticles on ZnO nanorods generate a high density of electromagnetic hotspots, enabling highly sensitive SERS detection (Fig. 2(m)). This approach enabled the clear detection of 20 nm PS, with a noticeable amplification of SERS signals upon the application of the pyroelectric potential (Fig. 2(n)).

Beyond detection capabilities, semiconductor-based substrates possess intrinsic photocatalytic properties that enable the light-driven degradation of surface-adsorbed organic contaminants, thereby realizing self-cleaning functionality [99–101]. This photocatalytic effect can also enhance Raman signals through photo-induced enhanced Raman scattering (PIERS), in which ultraviolet (UV) pre- or co-irradiation induces charge carrier migration and surface charge redistribution, leading to Raman intensities that can even surpass those of metallic SERS substrates. The PIERS strategy thus not only improves detection sensitivity but also facilitates *in situ* monitoring of NPs photodegradation kinetics. For instance, Olugbenga et al. [102] fabricated a PIERS substrate of flower-like Ag nanosheets on TiO_2, enabling detection of 20 nm PVC particles and real-time observation of their UV-induced degradation, with Raman signal enhancement up to ~ 2.6×10^2 compared to conventional SERS .

However, despite these functional benefits, pure semiconductor substrates generally exhibit weaker enhancement compared to noble metal-based substrates due to their low free-carrier density and limited plasmonic resonance. Their charge-transfer-dominated mechanism is highly sensitive to surface states, band alignment, and excitation wavelength, often resulting in poor signal reproducibility and limited applicability, posing challenges for scalable and consistent substrate fabrication [96].

3.2.4 *Enrichment strategies for NPs*

Given the extremely low abundance of NPs in environmental matrices and the susceptibility of their signals to noise interference, enrichment prior to detection represents a direct and effective strategy. Approaches such as hydrophobic interface trapping, optical manipulation, microfluidic concentration, and phase

separation can efficiently preconcentrate NPs without altering their intrinsic properties, thereby overcoming instrumental detection limits and facilitating subsequent compositional analyses.

1) **Optical manipulation enrichment:** Laser-induced localized photothermal and fluidic gradient effects in liquid media have emerged as a promising non-contact strategy for the enrichment and aggregation of NPs. Through thermophoretic effects, laser irradiation simultaneously concentrates analytes and forms dense SERS hotspots (Fig. 3(a)), where nanoparticle migration markedly amplifies Raman signals [103].

In a representative study, Moon et al. [104] proposed a unique shrinking surface bubble deposition (SSBD) technique for the collection and detection of NPs in seawater. In this process, seawater samples are mixed with silver nanoparticles and irradiated with a laser to generate microbubbles. As the bubbles shrink and collapse, the collected particles adhere to the substrate through van der Waals interactions (Fig. 3(b)), thereby significantly enhancing their detectability under scanning electron microscopy (SEM). Moreover, the co-deposited Ag nanoparticles provide SERS activity, which improves the chemical identification of trace-level NPs. Using this approach, both PS and PET NPs were successfully detected in seawater. Furthermore, Shi et al. [61] developed an optical manipulation (OM) combined with SERS (OM-SERS) system in which laser spot sizes can be adjusted, enabling simultaneous enrichment and quantification of NPs in natural waters while greatly reducing processing time. By adjusting the laser spot size, gold nanoparticle stacks (GNSs) of different dimensions were obtained: small-sized GNSs were optimized for trapping single NPs, whereas large-sized GNSs were utilized for enrichment and quantitative detection. Laser on/off modulation facilitated homogeneous mixing between NPs and Au nanoparticles, allowing for *in situ* SERS detection (Fig. 3(c)). Using this system, PS (6.5–8.5 $\mu g \cdot L^{-1}$) and PET (66 $\mu g \cdot L^{-1}$) NPs ranging from 45 to 273 nm were successfully detected in river water samples. In aquaculture and coastal seawater samples, concentrations of PS NPs were determined to be 1.4–1.8 and 0.7–1.0 $\mu g \cdot L^{-1}$, respectively, requiring only 7.2 mL of sample volume. When compared with conventional Py-GC/MS combined with filtration-based enrichment (using 100 nm membranes), the OM-SERS method yielded higher measured concentrations—likely due to NP losses during filtration in the traditional approach. This highlights the superior enrichment efficiency of the OM-SERS system and demonstrates its strong potential for applying SERS-based detection to real environmental samples.

Although optical manipulation offers non-contact and rapid aggregation of NPs, its performance is limited by laser power, uneven photothermal effects, system stability, and the complexity of natural waters. Future advances require low-power optical field designs, well-controlled thermo-fluidic environments, and scalable, interference-resistant optical platforms.

2) **Self-assembled monolayer enrichment:** The self-assembly strategy for constructing NPs–metal nanoparticle monolayers enables uniform nanoparticle distribution and dense plasmonic hotspots, markedly enhancing SERS sensitivity and reproducibility. The simple, liquid-phase process minimizes optical interference, ensures quantitative signal acquisition, and is compatible with diverse nanoplastic types. Yuan et al. [105] developed the co-assembly of silver nanoparticles and NPs into a monolayer film. Briefly, introducing Ag nanoparticles into the NP suspension initiates 1H,1H,2H,2H-perfluorodecanethiol (PFT)-mediated coassembly. PFT anchors to NPs via hydrophobic interactions and to Ag nanoparticles through thiol–metal bonding, driving both species to the hexane–water interface to form a coassembled monolayer. After transferring the film onto a silicon wafer, thermal treatment induces polymer fusion and creates Ag hotspots, enabling subsequent SERS analysis (Fig. 4(a)). Upon analysis, 80 nm PS exhibited a strong and concentration-dependent SERS response, with an LOD of 0.1 $mg \cdot L^{-1}$, while the LODs of 300 and 800 nm polymethyl methacrylate (PMMA) were 5 and 0.1 $mg \cdot L^{-1}$, respectively. Unlike earlier methods restricted to PS–Au assemblies (Fig. 4(b)) [106], this approach enables multicomponent and morphology-independent interfacial assembly, thereby broadening its applicability. Low-concentration PET NPs can also be detected using a similar approach [107]. However, the self-assembly of NPs with Au/Ag nanoparticles also has limitations. Organic molecules introduced during assembly may adsorb on surfaces, causing spectral interference and competing with analytes, which reduces signal reproducibility and SERS enhancement.

3) **Superhydrophobic surfaces enrichment:** On a superhydrophobic surface, evaporating droplets containing NPs form nearly spherical shapes, and interfacial tension and capillary forces drive the particles toward the droplet center, resulting in highly concentrated deposits (Fig. 4(c)). Xing et al. [108] developed a novel technique combining superhydrophobic enrichment with SERS for trace detection of NPs in water. The superhydrophobic gold nanoparticle substrate, fabricated via a liquid–liquid self-assembly method, efficiently concentrated NPs onto the SERS-active surface during droplet evaporation. This approach enabled

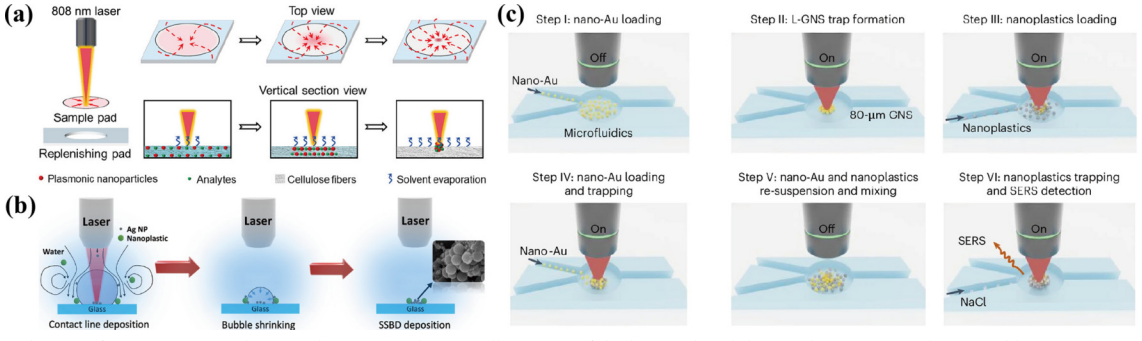

Figure 3 Enrichment of NPs using optical manipulation. (a) Schematic illustration of the laser-induced thermophoresis paper device enabling simultaneous plasmonic nanostructure formation and target enrichment. Reproduced with permission from Ref. [103], © American Chemical Society 2024. (b) Schematic of the SSBD process, in which a laser-induced thermal bubble drives thermofluidic flow to concentrate suspended particles and deposit them into a high-density spot once the bubble collapses. Reproduced with permission from Ref. [104], © Moon et al. 2024. (c) Schematic illustration of the microfluidic-assisted manipulation (enrichment) and SERS detection workflow for NPs. Reproduced with permission from Ref. [61], © Shi et al. 2025.

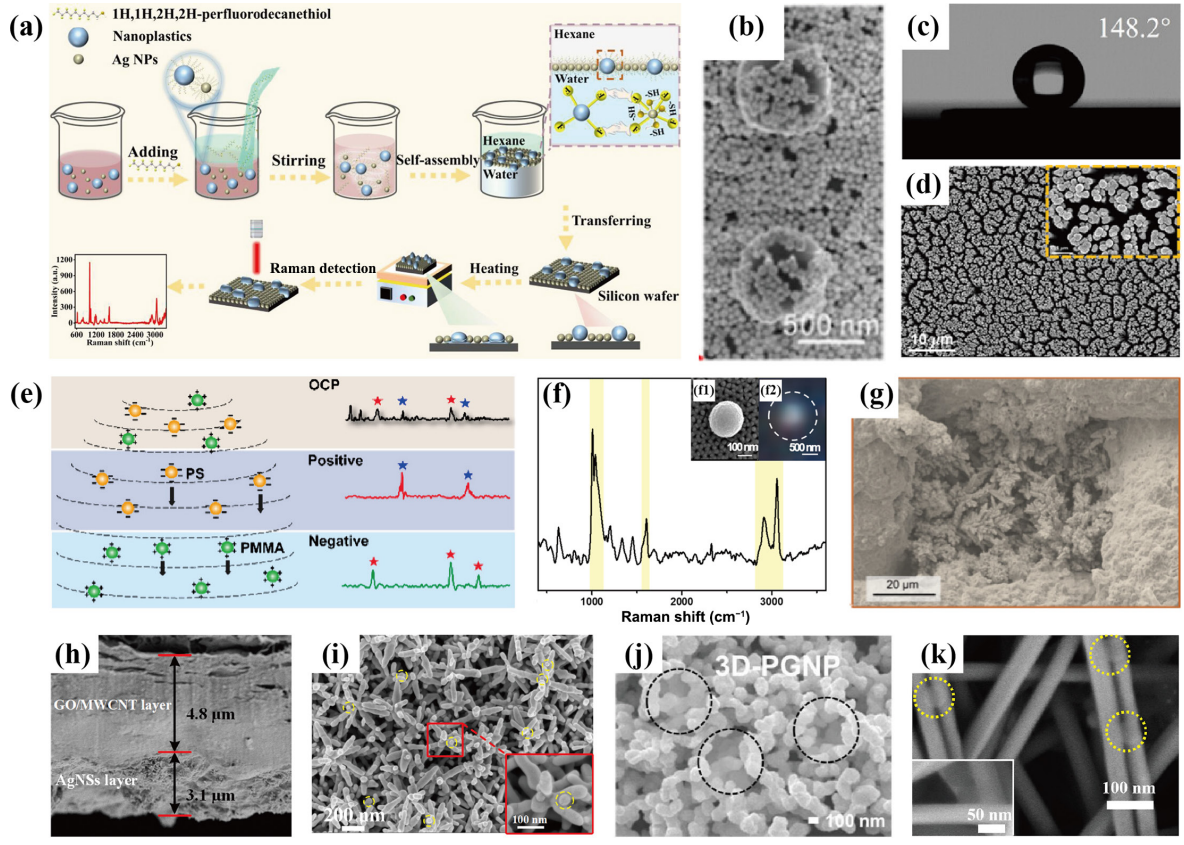

Figure 4 Enrichment of NPs by self-assembled monolayers, superhydrophobic surfaces, plasmonic coacervates and *in situ* enrichment. (a) Schematic illustration of SERS detection of NPs by the coassembly monolayer film. Reproduced with permission from Ref. [105], © American Chemical Society 2025. (b) SEM image of Au nanoparticle encapsulation of NPs with strong interparticle coupling. Reproduced with permission from Ref. [106], © American Chemical Society 2023. (c) Contact angles of water droplets on superhydrophobic Au nanoparticle substrates. Reproduced with permission from Ref. [108], © American Chemical Society 2025. (d) Top-view SEM images of SERS substrate with high-density hotspots fabricated via AAO templating and subsequent metal sputtering. Reproduced with permission from Ref. [114], © Kim et al. 2025. (e) Electrokinetic schematic illustrating the preferential interfacial adsorption of PS and PMMA under an electric field gradient (dotted lines). Reproduced with permission from Ref. [111], © American Chemical Society 2025. (f) Raman spectra of 200 nm PS on a 20 nm pore AAO membrane. (f1) SEM image of 200 nm PS on 20 nm pore AAO. (f2) Dark-field image of 200 nm PS on 20 nm pore AAO. Reproduced with permission from Ref. [115], © Elsevier Ltd. 2025. (g) SEM image of a nanoporous SERS membrane capable of filtering and detecting airborne NPs. Reproduced with permission from Ref. [117], © American Chemical Society 2024. (h) Cross-sectional SEM image of the GO/MWCNT–AgNS membrane and (i) SEM image of 50 nm PS enriched on GO/MWCNT–AgNS membranes. Reproduced with permission from Ref. [118], © Elsevier Ltd. 2024. (j) SEM image of the structure of 3D plasmonic gold nanopockets. Reproduced with permission from Ref. [119], © Kim et al. 2023. (k) SEM image of 50 nm standard PS retained on the membrane. Reproduced with permission from Ref. [120], © American Chemical Society 2022.

the detection of 30–1000 nm PS at concentrations as low as 0.03 μg·mL^{-1} in a 10 μL of water. The method was further applied to the detection of PET NPs in bottled water, demonstrating excellent sensitivity, reproducibility, and temporal stability.

4) **Plasmonic coacervate enrichment:** Coacervates provide a confined, hydrophobic microenvironment that efficiently concentrates target molecules. While initially applied primarily in biocatalysis and biosensing [109], these enrichment properties also confer strong potential for the selective capture and sensitive detection of NPs. Ning et al. [110] employed plasmonic coacervate microdroplets encapsulating silver nanoparticles (AgNPs) to enhance SERS signals. Aggregation of AgNPs within the coacervates generates numerous plasmonic "hotspots", while the partially dehydrated and hydrophobic interior efficiently enriches target analytes. This strategy enabled sensitive detection of low-concentration PS, including 20 nm (0.05 ppb) and 50 nm (0.5 ppb) particles.

5) ***In situ* enrichment:** The *ex situ* enrichment strategies discussed above suffer from sample loss and selective particle capture. In contrast, *in situ* enrichment and detection better preserve the native composition and distribution of NPs. Li et al. [111] introduce a miniaturized electrochemical SERS platform integrating a one-step–fabricated poly(vinyl alcohol oxide)-gold nanoparticle (AuNPs) hydrogel, enabling electrokinetic enrichment and *in situ* Raman analysis of NPs in real samples. The 3D porous hydrogel provides a confined, optically transparent matrix that supports uniform *in situ* growth and dispersion of AuNPs, suppresses aggregation, and yields more homogeneous hotspots, thereby improving excitation efficiency, signal intensity, and analytical reproducibility. Negatively charged PS (100 nm) and positively charged PMMA (150 nm) exhibited opposite signal responses to applied potential polarity (Fig. 4(e)), enabling selective and reversible detection with LODs of 1.01 and 0.45 μg·mL^{-1}, respectively. Furthermore, a rapid *in situ* Raman technique integrating dielectrophoresis and alternating current (AC) electroosmosis mitigates diffusion constraints and enhances weak Raman signals of NPs in aqueous environments via SERS amplification, markedly improving detection efficiency [112]. The LOD for 30 nm PS using gold nanorods was determined to be 1.17 μg·L^{-1}.

3.2.5 *Filter-type SERS sensor*

Filtration serves as an effective enrichment strategy for SERS analysis. Integrating filtration and detection functions into a single SERS platform enables *in situ* analysis. Filter-type SERS substrates embed plasmonic nanostructures on porous membranes, enabling concurrent particle capture and signal enhancement while avoiding losses from separate pretreatment steps. These flexible, low-cost, and disposable membranes are ideal for rapid on-site screening. The following section classifies SERS substrates based on their supporting materials.

1) **AAO membranes.** AAO membranes are low-cost, precisely tunable nanostructured materials characterized by highly ordered nanopores that facilitate size-selective filtration and directional enrichment of NPs. Such confinement promotes localized hotspot formation, markedly enhancing Raman signals. Their large surface area, chemical stability, and compatibility with noble metals (e.g., Au, Ag) make them ideal for online and high-throughput SERS analysis [113]. Moreover, AAO serves as a versatile template for fabricating ordered nanostructures (Fig. 4(d)) [89, 114]. Seo et al. [115] first detected individual NPs using unmodified AAO membranes with 20 nm pores (Fig. 4(f)), yielding optimal Raman enhancement for 200 nm PS and other polymers. This substantially reduces the cost associated with noble-metal coating. Wu et al. [88] integrated AAO with algorithm-assisted classification for precise identification, while Ruan et al. [116] employed Au-coated AAO to detect PS down to 200 nm and other NPs in sea salt.

2) **Metallic membranes.** While AAO membranes are widely used as SERS supports, their brittleness limits mechanical stability. In contrast, metal-based substrates offer higher strength and pressure resistance, enabling continuous enrichment and online monitoring under high-flow or high-pressure conditions. For instance, Kim et al. [117] electrodeposited anisotropic nanodendrites on copper mesh (Fig. 4(g)), followed by a rolling treatment at 160 kgf and Au coating to enhance durability and SERS performance. Designed for airborne particle capture, the membrane achieved 95.9% filtration efficiency for 300 nm KCl particles at 5 kV with a pressure drop of 121 Pa. Crucially, it successfully detected 100 nm PS at 50 μg·mL^{-1}. It also maintained structural integrity after ethanol washing and 22,000 fatigue cycles at 177 kPa, showing no detectable signal degradation.

3) **Polymeric membranes.** This type of membrane, featuring tunable structures, adjustable surface chemistry, and mechanical flexibility, provides a versatile platform for integrated SERS detection and enrichment. Recent studies have commonly integrated synthetically prepared metallic nanoparticles onto membrane substrates, markedly enhancing SERS performance. For instance, Jiang et al. [118] sequentially deposited graphene oxide (GO), aqueous dispersions of multi-walled carbon nanotubes (MWCNTs), and silver nanostars (AgNSs) colloidal solutions onto a cellulose acetate (CA) membrane (Figs. 4(h) and 4(i)), fabricating a composite film (GO/MWCNT–AgNS). The SERS membrane enables 97.1% retention of 50 nm PS with an LOD of 5×10^{-5} mg·mL^{-1}. Similarly, Kim et al. [119] prepared 3D porous Au nanoparticle films on CA filters (Fig. 4(j)) for syringe-based filtration–detection. Yang et al. [120] assembled Ag nanowires (AgNWs) on PTFE membranes (Fig. 4(k)) for imaging and quantification of PS (LOD = 10^{-7} g·L^{-1}) and PMMA (LOD = 10^{-6} g·L^{-1}), including those released from expanded polystyrene containers. In another study, Yang et al. [121] immobilized Ag nanoparticles of two sizes (Ag-250 and Ag-125) on polyvinylidene fluoride (PVDF) membranes in a checkerboard pattern, enabling the detection of 100 nm PS spiked in tap and lake water.

While filters can enrich NPs for detection, complex sample matrices pose major challenges. Organic matter, salts, and colloids in environmental or biological samples may compete for SERS-active sites, weakening signals or causing fluorescence interference. Moreover, the instability of the metal layer during prolonged filtration can lead to detachment or deformation, diminishing enhancement. Consequently, priorities for future SERS detection based on membrane-assisted enrichment should focus on substrates with improved stability and optimized structural design. Constructing three-dimensional hierarchical porous architectures can simultaneously enhance analyte enrichment and electromagnetic field coupling. In addition, engineering anti-fouling, mechanically fatigue-resistant, and reusable membrane–SERS hybrid interfaces will further improve their reliability in real-sample applications.

3.3 High-speed particle imaging

High-quality nanoplastic imaging hinges on achieving high-resolution, high-signal-to-noise detection under nondestructive, stable, and well-dispersed sample conditions. Achieving this standard requires advanced high-resolution detectors, low-noise acquisition electronics, nanoscale positional stability, and dedicated hardware capable of preserving sample integrity throughout measurement. Among various analytical techniques, Raman spectroscopy stands out for its label-free capability, molecular fingerprint specificity, and suitability for *in situ* measurements in wet or complex matrices. Linear Raman is simple, broadly applicable, and provides comprehensive spectral information, albeit with limited sensitivity. In contrast, nonlinear Raman achieves ultrahigh signals and rapid imaging at the cost of complexity and narrower spectral range. Ultimately, the strategic combination of these modes balances sensitivity with practicality.

3.3.1 *Linear Raman spectroscopy*

Conventional Raman imaging relies on point-by-point scanning of a focused laser beam to collect scattered spectra, but its weak signal leads to slow acquisition and susceptibility to fluorescence interference. To address these issues, wide-field hyperspectral imaging enables simultaneous spatial–spectral acquisition under wide-field illumination, capturing complete spectra for each pixel. This approach minimizes scanning time and signal drift while offering high sensitivity, stability, and multicomponent identification capability. In a notable study, Ardini et al. [122] developed a wide-field hyperspectral Fourier-transform Raman system for rapid imaging and identification of NPs. The setup employs an ultrastable birefringent interferometer (TWINS) that splits the incident wavefront into two collinear, time-delayed replicas, enabling parallel spectral acquisition across all pixels. Short- and long-pass filters effectively eliminate residual excitation light and fluorescence background, while adjustable scanning ranges enable precise separation of Raman and fluorescence signals. The system demonstrates high spatial (~ 1 μm) and spectral (~ 23 cm^{-1}) resolution, acquiring 100,000-pixel images in ~ 15 min—a significant improvement over the hours required by conventional point-scanning Raman (Fig. 5(a)). This capability allows for the direct detection of NPs in complex, untreated environmental samples. However, although hyperspectral imaging has reached a high degree of technological maturity, its application to

nanoparticle detection remains limited, constrained by the demanding requirements for sensitivity, stability, and system compactness [123]. Alternatively, Wu et al. [124] developed a line-scan confocal Raman microscopy system. This setup utilizes a cylindrical lens for line illumination combined with a Powell lens to ensure a uniform intensity distribution along the excitation line. This configuration enables rapid imaging and chemical identification of NPs down to 200 nm, completing a 40 μm × 10 μm scan within 10 s (500 nm step size, 0.5 s exposure per step) (Fig. 5(b)). Compared with conventional point-scanning Raman microscopy (tens of minutes), this approach enhances imaging speed by one to two orders of magnitude.

3.3.2 *Nonlinear Raman spectroscopy*

Coherent anti-Stokes Raman scattering (CARS). CARS has been developed to address the inherently weak signal intensity and slow acquisition speed of spontaneous Raman spectroscopy. Based on the principle of four-wave mixing, when the frequency difference between the pump (ω_p) and Stokes (ω_s) beams matches a molecular vibrational frequency, a high-energy anti-Stokes signal ($2\omega_p-\omega_s$) is generated. This signal appears at shorter wavelengths, effectively minimizing fluorescence interference from samples and thereby making CARS particularly suitable for fluorescent materials (Fig. 5(c)). In addition, its strong directionality, high signal intensity, and excellent temporal resolution enable rapid Raman imaging at sub-second or even video-rate acquisition speeds. Recent studies have demonstrated the use of CARS for rapid imaging of MNPs smaller than 10 μm [125, 126], real-time identification of MNPs in flow [127, 128], and dynamic tracking of PS MNPs and lipid droplets within living cells [129]. These advancements are pivotal for *in situ* monitoring of NPs in liquid environments, as well as for elucidating their intracellular dynamics and cytotoxic mechanisms. Although studies on NPs smaller than 1 μm remain limited, the technique exhibits strong potential—for example, Choi et al. [129] achieved rapid imaging of 830 nm lily pollen grains (Fig. 5(d)), demonstrating the feasibility of submicron-scale CARS detection.

Stimulated Raman scattering (SRS): Compared with CARS, SRS offers distinct advantages, particularly its ability to provide background-free imaging with linear quantitative capability. SRS operates through energy exchange between the pump and Stokes beams. When their frequency difference resonates with a molecular vibrational mode, the pump beam undergoes a slight attenuation (stimulated Raman loss, SRL), while the Stokes beam experiences a corresponding amplification (stimulated Raman gain, SRG). Crucially, the magnitude of this intensity change is linearly proportional to molecular concentration, which simplifies data interpretation and facilitates rapid, precise quantitative analysis. To date, SRS has been successfully employed to detect nanoscale NPs under a variety of experimental conditions.

Ao et al. [130] established a 3D SRS microscopy method for single-particle imaging of NPs and MPs. By scanning the

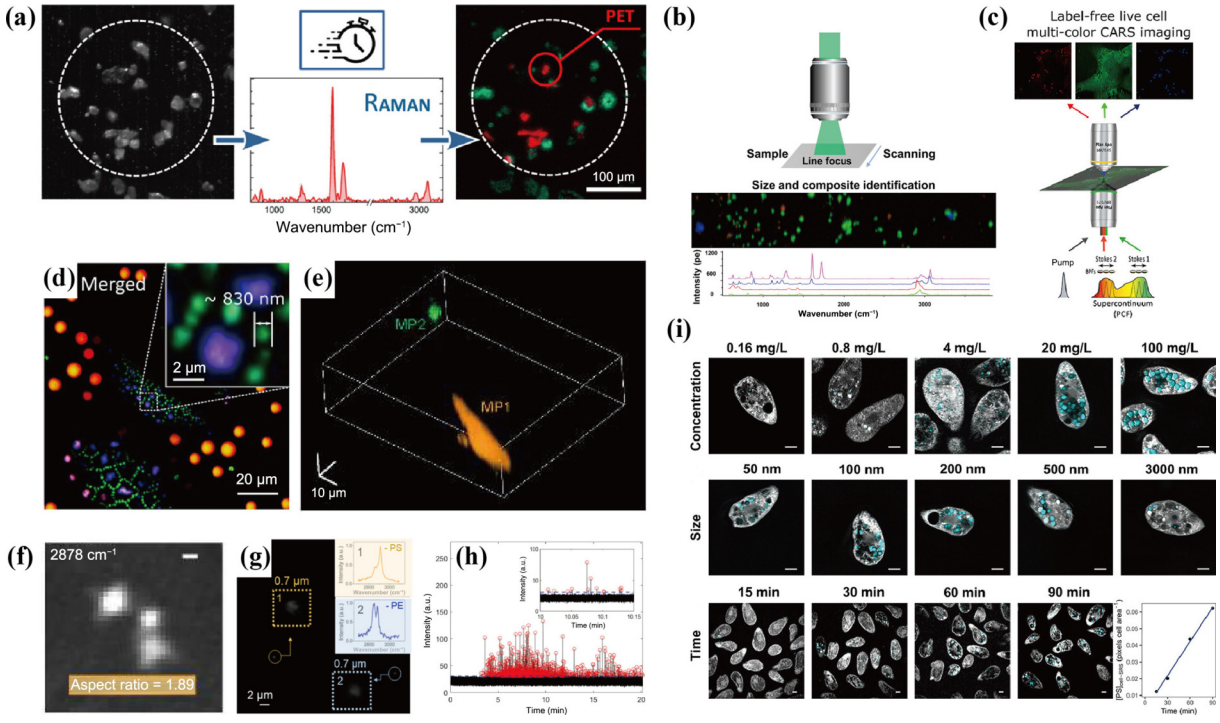

Figure 5 Rapid imaging of NPs using linear and nonlinear Raman spectroscopy. (a) Schematic of wide-field Fourier transform Raman microscopy for rapid imaging of different NPs. Reproduced with permission from Ref. [122], © Ardini et al. 2025. (b) Schematic of line-scan Raman micro-spectroscopy for rapid imaging of different NPs. Reproduced with permission from Ref. [124], © Wu et al. 2024. (c) Schematic of label-free multicolor Coherent anti-Stokes Raman scattering microscopy for rapid imaging of different particles and (d) the multicolor CARS imaging of the PS beads (orange), pollen grains (green), and pollenkitt (purple). Reproduced with permission from Ref. [129], © American Chemical Society 2022. (e) 3D image of NPs/MPs found in an atmospheric sample. Reproduced with permission from Ref. [130], © Ao et al. 2023. (f) Representative SRS images of plastic particles with specific shapes indicated by aspect ratios. Scale bar, 0.6 μm. Reproduced with permission from Ref. [131], © Qian et al. 2024. (g) SRS imaging and spectra of NPs in sea salt samples. Reproduced with permission from Ref. [116], © American Chemical Society 2024. (h) Detection of 250 nm PS in a flow-cell using SRS (at 3049 cm^{-1}). Each red circle represents an event (the detection of NPs indicated by peaks). The blue dotted line represents the threshold, which is the minimum peak height required for counting. Reproduced with permission from Ref. [132], © Huber et al. 2024. (i) SRS imaging of *T. thermophila* at different PS concentrations, different PS sizes and different exposure time. Reproduced with permission from Ref. [133], © American Chemical Society 2024.

2750–3050 cm^{-1} region and validating at lower wavenumbers, they detected NPs as small as 100 nm and identified PP, PE, and cellulose NPs in human lung tissue. Notably, this strategy enables the reconstruction and visualization of the 3D structure of NPs encompassing fibrous, fragmental, and granular forms (Fig. 5(e)), thereby offering new insights into their morphology-dependent environmental behaviors. Similarly, Ruan et al. [116] employed SRS imaging to quantify NPs in sea salt from multiple regions, completing a 1248 μm^2 scan within 2 min and detecting particles as small as 500 nm PE, 700 nm PS (Fig. 5(g)), and 800 nm PP. Estimates suggest that annual human intake via sea salt reached up to 6 million particles. Building on this high-speed capability, Qian et al. [131] integrated narrowband SRS with an automated identification algorithm, enabling high-throughput, chemically specific single-particle analysis. Strategically focusing excitation on characteristic vibrational modes with large Raman cross-sections greatly enhanced sensitivity, permitting the detection of NPs down to 100 nm. When applied to bottled water, this approach uncovered a particle concentration of $(2.4\pm1.3)\times10^5$ particles·L^{-1}, of which ~ 90% were NPs, a figure several orders of magnitude higher than prior estimates. The high-throughput analysis also exposed strong heterogeneity between polymer composition and particle morphology (Fig. 5(f)). This capability enables a transition from macroscopic ensemble analysis to a more refined investigation of single-particle behaviors and formation mechanisms within complex systems. Huber et al. [132] validated the SRS detection of flowing NPs (100–5000 nm, PE, PMMA, PS), capturing single-particle signals within 60.5 μs and correlating particle counts with mass concentration. Crucially, the technique discriminated between optically trapped and free particles based on signal profiles, while the quantitative analysis of signal width and intensity enabled particle size estimation (Fig. 5(h)). This method provides a foundation for rapid *in situ* quantification and compositional analysis of NPs, holding strong potential for environmental monitoring and pollutant tracking. Extending into biological domains, SRS has also been effectively applied for the label-free detection of NPs in biological systems. Wang et al. [133] differentiated various NPs (PE, PET, PMMA, PP, PS, PVC) via characteristic SRS spectra (Fig. 5(i)), enabling the identification of individual and mixed NPs in protozoa. In a toxicological context, Xin et al. [134] used hyperspectral SRS microscopy to quantify the bioaccumulation and toxicity of NPs in zebrafish. Their study revealed that 50 nm PS induced stronger hepatic inflammation and accumulated in the brain and vascular walls, indicating potential cardiovascular toxicity and thrombus risk.

SRS offers groundbreaking potential in signal enhancement and real-time imaging, advancing the detection of NPs from static analysis to *in situ* and dynamic characterization, thereby providing new technological avenues for elucidating toxicological mechanisms of NPs.

3.4 *In situ* multimodal detection

In situ multimodal detection can be considered as a key future direction for NPs analysis. By integrating complementary analytical techniques within a single microenvironment, researchers can simultaneously capture structural, chemical, and physical information. This approach provides a comprehensive understanding of NPs aging, adsorption, and interfacial behaviors in complex media.

AFM+IR: AFM enables precise mapping of NPs surface morphology, roughness, mechanical properties, and adhesion forces [135–138]. To acquire chemical information, AFM has been coupled with infrared spectroscopy (AFM+IR). In a notable application, Belontz et al. [139] combined AFM+IR and optical photothermal IR (O-PTIR) to detect and quantify NPs in environmental samples, including poly(3-hydroxybutyrate-co-4-hydroxybutyrate) (P(3HB-co-4HB)). Their study revealed that 96% of particles exhibited a thickness < 1 μm, with the smallest particle height measured at 14 nm (Fig. 6(a)). Li et al. [140] used AFM+IR to confirm the presence of PE and PVC NPs in drinking water treatment plants, identifying 200 nm particles via AFM and their polymer types via IR, highlighting oxidation units as potential NPs sources. Furthermore, Xie et al. [141] directly identified individual 300 nm poly(3-hydroxybutyrate) (P3HB) and 860 nm bisphenol-A-based epoxy resin particles in environmental water, simultaneously obtaining crystallinity information to study oxidation and degradation processes. Finally, Luo et al. [142] prepared nano-TiO_2-coated PP and applied AFM+IR to systematically investigate nanoscale infrared, thermal, and mechanical properties before and after photodegradation, revealing that photocatalytic reactions accelerated aging and significantly altered the plastics' physicochemical characteristics.

SEM+Raman: SEM is capable of visualizing nanoscale plastic particles and surface features that are beyond the resolution limit of conventional optical microscopy. A non-destructive analytical method combining Raman imaging with SEM (RISE) was applied to directly identify and characterize nanoparticles on the surface of recycled PVC powders. This approach enables simultaneous acquisition of morphological and chemical information at the single-particle level. Automated RISE mapping provides two-dimensional chemical composition of selected regions (Fig. 6(b)), effectively distinguishing PVC from other components without colloidal separation [143].

Furthermore, coupling SEM with SERS allows for higher-resolution identification of individual NPs by integrating the ultrahigh spatial resolution of SEM with the molecular fingerprinting capability of Raman spectroscopy for single-particle analysis (Fig. 6(c)) [144].

IR+Raman: IR and Raman spectroscopy are complementary techniques based on different molecular vibration mechanisms: IR is sensitive to changes in dipole moment, whereas Raman depends on variations in polarizability. In plastic analysis, IR excels at identifying oxygen-containing functional groups, while Raman is more responsive to C–C and C–H backbone vibrations. Their combined application enables full-spectrum coverage of molecular vibrations, enhancing the accuracy and completeness of chemical identification [145]. Recently, the computer-controlled optical photothermal IR coupled with Raman (CC-O-PTIR+Raman) technique was first applied to characterize aerosolized microplastic particles, simultaneously characterizing MPs (≤ 10 μm) and NPs (Fig. 6(d)) [146]. Automated analysis significantly improved efficiency and extended the applicability of IR spectroscopy to sub-10-μm particle analysis.

In situ multimodal characterization integrates techniques like Raman, IR, and AFM to simultaneously capture chemical, structural, and mechanical information. However, developing such systems requires overcoming challenges in complex optical coupling and multi-source data synchronization, resulting in long research and development (R&D) cycles. Additionally, multimodal platforms often involve custom high-precision components and

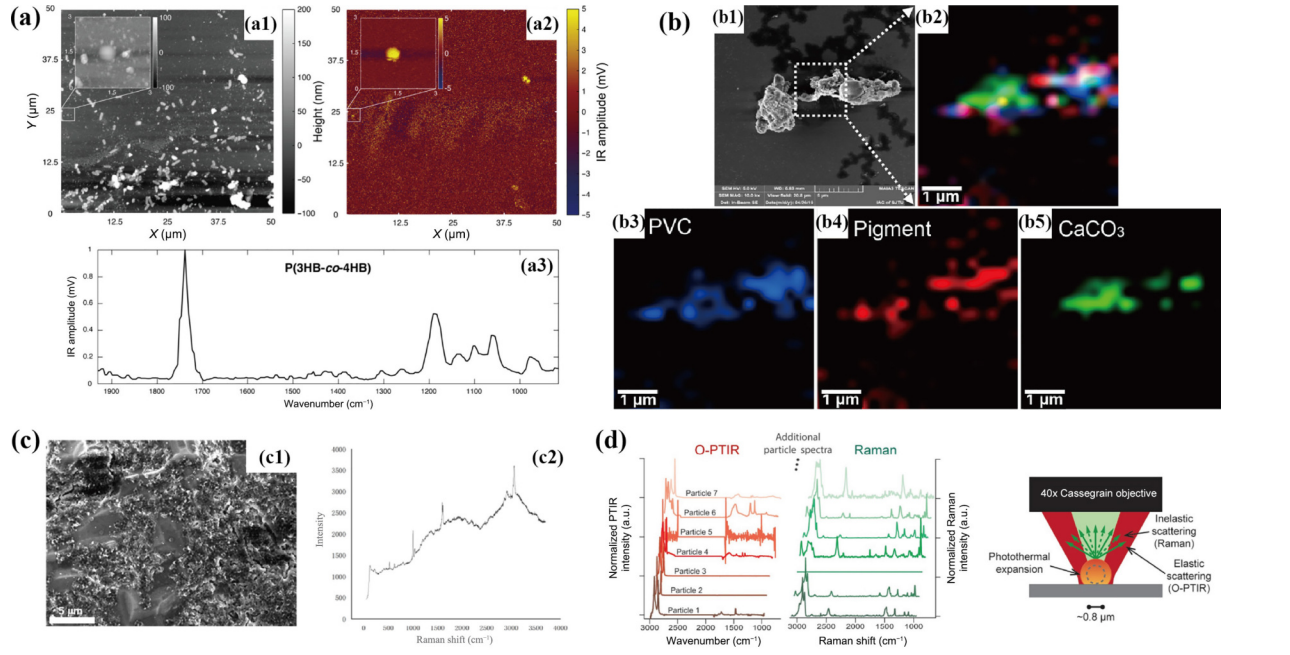

Figure 6 *In situ* multimodal detection of NPs. (a) AFM-IR spectroscopy measurement of snowmelt from Beaver Mountain. (a1) AFM-IR topography map and (a2) IR absorption map at 1735 cm^{-1}, corresponding to polyester. (a3) The corresponding P(3HB-co-4HB) spectrum. Reproduced with permission from Ref. [139], © Belontz et al. 2025. (b) Raman spectral mapping of nanoparticles released from recycled PVC powders. Reproduced with permission from Ref. [143], © American Chemical Society 2020. (c): (c1) SEM image and (c2) Raman spectrum of particles identified as PS from a tissue sample. Reproduced with permission from Ref. [144], © Elsevier B.V. 2022. (d) Schematic diagram of detecting NPs using coupled O-PTIR and Raman spectroscopy. Reproduced with permission from Ref. [146], © American Chemical Society 2025.

advanced control systems, making initial development and maintenance costs significantly higher than single-modality instruments. Despite clear performance advantages, their large-scale deployment remains limited by cost and engineering maturity, restricting their use primarily to research laboratories rather than routine detection scenarios.

4 Conclusion and outlook

The landscape of NPs detection is undergoing a pivotal shift—moving from isolated methodological breakthroughs toward a more systematic, performance-driven paradigm. While early studies focused primarily on proving feasibility, the current frontier demands superior throughput, precision, and comprehensive characterization. Given the ultra-trace concentrations, polydisperse distributions, and the intrinsic complexity of environmental matrices, it is increasingly evident that no single analytical modality can capture the full physicochemical picture. Instead, future progress hinges on synthesizing these methods and establishing multidimensional evaluation frameworks.

This evolution demands profound interdisciplinary synergy. It requires integrating robust pretreatment strategies, sensitive spectroscopy, and precise optical manipulation with the enrichment capabilities of microfluidics and the data-mining power of artificial intelligence. In terms of specific techniques, mass spectrometry remains the gold standard for accurate quantification in complex matrices, though it inevitably sacrifices morphological integrity. Conversely, Raman spectroscopy and its derivatives—such as SERS and SRS—offer exceptional potential for *in situ* visualization and multimodal characterization. Finally, while machine learning provides a powerful toolkit for signal extraction, its success is predicated on the quality of the underlying data. Consequently, we urge the academic community to accelerate the creation of shared, standardized spectral databases, which will serve as the linchpin for training the next generation of intelligent detection models.

To accelerate the deployment of NPs detection in real-world scenarios, we introduce a standardized quantitative framework designed to rigorously assess analytical performance and ensure inter-laboratory comparability. We introduce the R^3ES evaluation model (Table 1), encompassing five key dimensions: Rapidness, Resolution, Reliability, Economy, and Sustainability. Rapidness captures detection speed and throughput; Resolution reflects spatial and precision; Reliability evaluates reproducibility and resistance to interference; Economy considers cost and operational complexity; and Sustainability assesses the environmental friendliness and reusability of reagents and consumables. Applying this framework, we assessed representative studies. However, due to the scarcity of data disclosed in earlier research, our evaluation focuses exclusively on the three core dimensions of Rapidness, Resolution, and Reliability, utilizing key metrics for analysis (Table 2). It is evident that select outstanding works have achieved an optimal trade-off between detection rapidity and sensitivity, serving as a robust benchmark for future advancements. Broadly, current literature suffers from inadequate data disclosure. Cross-study benchmarking is severely impeded by size-induced fluctuations in LOD and the absence of standardized reporting units. Similarly, critical efficiency metrics, specifically pretreatment and detection durations, are frequently omitted despite their importance for evaluating practical utility. Moreover, the predominant reliance on PS microspheres necessitates an urgent expansion to diverse polymer types. Consequently, the path toward standardized, real-world NPs detection remains arduous.

This framework is envisioned to guide the rational design of high-performance, eco-friendly, and practical detection systems, catalyzing the transition of nanoparticle detection from exploratory

Table 1 Quantitative evaluation framework for NPs detection techniques (R^3ES)

Primary dimension	Secondary indicator	Quantifiable parameter
R1—Rapidness	(1) Single measurement time	Time required to complete one test (min·sample^{-1})
	(2) Sample throughput	Number of samples analyzed per hour (samples·h^{-1})
	(3) Degree of automation	Presence of automated sample feeding and data analysis (score: 0–1 or qualitative: low/medium/high)
R2—Resolution	(1) Minimum detectable particle size	(nm)
	(2) LOD	minimal concentration of detection (μg·L^{-1})
	(3) SNR or enhancement factor (EF)	SNR or EF (expressed as $\log_{10}$)
R3—Reliability	(1) Repeatability	Relative standard deviation (RSD) (%)
	(2) Anti-interference capability	A semi-quantitative score (1–5) evaluates the anti-interference capability in realistic matrices: Score 1 (ideal): Milli-Q/spiked water; Score 2 (simple): TAP/rainwater; Score 3 (surface): river/lake/seawater; Score 4 (complex fluids): wastewater/beverages/biofluids; Score 5 (solid matrices): sludge/soil/tissue.
	(3) Stability of detection limit	(ΔLOD/LOD$_0$): Variation in LOD across different batches (%)
E—Economy	(1) Instrument cost	Equipment cost (10^3–10^5 USD or in RMB×10^4)
	(2) Consumable cost	Cost per sample (USD·sample^{-1})
	(3) Operational complexity	Evaluated by number of procedural steps or rating scale (1–5, 1 = simple, 5 = complex)
	(4) Sample pretreatment time	Preparation time per sample (min·sample^{-1})
S—Sustainability	(1) Environmental greenness	Requirement for strong acids or organic solvents (qualitative score: 0–1)
	(2) Sample destructiveness	Whether sample can be reused (0 = destructive; 1 = non-destructive)

Table 2 Summarization of different techniques applied to the identification of NPs

No.	Technological type	Plastic type	Resolution		Rapidness	Reliability		Ref.
			LOD	Minimum detectable particle	Single measurement time	Anti-interference capability	Qualitative capability	
1	Optical sieve	PS	NA[b]	200 nm	> 2 min	3	Physical	[70]
2	SP-ICP-MS	PS	7.1×10^6 particles·L^{-1}	800 nm	NA[b]	2	Elemental analysis	[75]
3	FI-MS	PS	0.7 μg	100 nm	Pretreatment < 20 min, analysis time < 50 s	5	Chemical	[86]
4	NEMS-MS	PS	NA[b]	100 nm	Analysis time of < 30 min	1	Physical	[87]
5	SERS[a]	PS	150 ng·L^{-1}	30 nm	360 min	3	Chemical	[61]
		PMMA	80 μg·L^{-1}	320 nm	360 min			
		PET	50 μg·L^{-1}	750 nm	360 min			
6	SERS	PS	0.5 μg·L^{-1}	300 nm	Pretreatment > 720 min, analysis time per pixel < 0.1 s	3	Chemical	[88]
7	SERS	PS	0.001%	50 nm	Analysis time per pixel < 10 s	2	Chemical	[90]
8	SERS	PS	0.1 ppm	50 nm	30 min	3	Chemical	[93]
		PMMA	1 ppm	500 nm				
		PE	5 ppm	740–4990 nm				
		PLA	1 ppm	250 nm				
9	SERS	PS	0.001%	20 nm	NA	1	Chemical	[98]
10	SERS	PS	1 μg·μL^{-1}	60 nm	~ 4 min	3	Chemical	[103]
11	SERS[a]	Nylon nanofibers	NA[b]	Diameters ~20 nm, lengths > several micrometers	> 120 min	3	Chemical	[104]
		PS	NA[b]	< 1 um				
		PET	NA[b]	~ 1 μm				
12	SERS[a]	PS	0.1 mg·L^{-1}	80 nm	NA[b]	3	Chemical	[105]
13	SERS[a]	PS	0.03 μg·mL^{-1}	30 nm	Pretreatment ~ 3 days, analysis time < 5 s	3	Chemical	[108]
14	SERS	PS	0.45 μg·mL^{-1}	100 nm	NA[b]	3	Chemical	[111]
		PMMA	0.8 μg·mL^{-1}	150 nm	NA[b]	3	Chemical	
15	SERS	PS	NA[b]	200 nm	Analysis time = 30 s	3	Chemical	[115]
16	SERS	PS	50 μg·mL^{-1}	100 nm	Pretreatment > 100 s, analysis time 3 s	1	Chemical	[117]

(Continued)

No.	Technological type	Plastic type	Resolution		Rapidness	Reliability		Ref.
			LOD	Minimum detectable particle	Single measurement time	Anti-interference capability	Qualitative capability	
17	SERS	PS	0.05 μg mL^{-1}	50 nm	NA[b]	3	Chemical	[118]
18	SERS	PS	25 μg·mL^{-1}	1 μm	NA[b]	3	Chemical	[119]
19	SERS[a]	PS	10^{-7} g·L^{-1}	50 nm	NA[b]	3	Chemical	[120]
20	FT-HSM[a]	PS and PMMA	NA[b]	3 μm	~ 15 min for a 100 kpixel image	5	Chemical	[122]
21	Line-scan Raman	PS	NA[b]	200 nm	Imaging a 40 μm ×10 μm area takes 10 s	1	Chemical	[124]
22	SRS[a]	PS	NA[b]	100 nm	Imaging a 89.6 μm × 89.6 μm takes 1.2 s	5	Chemical	[130]
23	SRS[a]	PS	NA[b]	60 nm	Imaging a 0.2 mm × 0.2 mm area takes 30 min	2	Chemical	[131]
24	SRS	PS and PMMA	NA[b]	100 nm	20 min SRS scan (60.5 μs acquisition)	1	Chemical	[132]
25	SRS	PS	0.16 mg·L^{-1}	50 nm	Inspecting 100 protozoan cells for NPs takes around 1–2 days	3	Chemical	[133]

[a]means the method successfully detected NPs in the environment; [b]NA means not reported; the scoring criteria for anti-interference capability are detailed in Table 1.

research toward standardized, verifiable applications. Such progress will expedite the development of low-cost, portable, and sustainable analytical platforms, ultimately facilitating comprehensive environmental and health risk assessments of NPs.

Data availability

All data needed to support the conclusions in the paper are presented in the manuscript. Additional data related to this paper may be requested from the corresponding author upon request.

Acknowledgements

The authors gratefully acknowledge financial support from the National Natural Science Foundation of China (Nos. 22376028, 22176036, 21976030, 22006020, and 223B2601).

Declaration of competing interest

All the contributing authors report no conflict of interests in this work.

Author contribution statement

J. L. W.: data curation, writing manuscript. M. L. M.: writing manuscript. L. C. W.: writing manuscript. Y. J. Y.: writing manuscript. L. W. Z.: project administration, supervision. All the authors have approved the final manuscript.

Use of AI statement

None.

References

[1] Akbari Dana, P.; Gaga, E. O.; Gedik, K. Analytical challenges and strategies for particle-based analysis of airborne micro(nano)plastics in size-fractionated samples using microscopy, SEM/EDX, and Raman spectroscopy. *Anal. Chem.* **2024**, *96*, 20622–20634.

[2] Luo, X.; Wang, Z. Q.; Yang, L.; Gao, T. G.; Zhang, Y. L. A review of analytical methods and models used in atmospheric microplastic research. *Sci. Total Environ.* **2022**, *828*, 154487.

[3] dos Santos Galvão, L.; Fernandes, E. M. S.; Ferreira, R. R.; dos Santos Rosa, D.; Wiebeck, H. Critical steps for microplastics characterization from the atmosphere. *J. Hazard. Mater.* **2022**, *424*, 127668.

[4] Shruti, V. C.; Pérez-Guevara, F.; Elizalde-Martínez, I.; Kutralam-Muniasamy G. Current trends and analytical methods for evaluation of microplastics in stormwater. *Trends Environ. Analy. Chem.* **2021**, *30*, e00123.

[5] Biao, W.; Hashim, N. A.; Rabuni, M. F. B.; Lide, O.; Ullah, A. Microplastics in aquatic systems: An in-depth review of current and potential water treatment processes. *Chemosphere* **2024**, *361*, 142546.

[6] Al Alwan, B.; Ismail, B.; El Jery, A.; Badawi, A. K. State-of-the-art strategies for microplastics mitigation in aquatic environments: Identification, technological innovations, and prospects for advancement. *J. Water Process Eng.* **2024**, *61*, 105336.

[7] Nawab, J.; Khan, H.; Ghani, J.; Zafar, M. I.; Khan, S.; Toller, S.; Fatima, L.; Hamza, A. New insights into the migration, distribution and accumulation of micro-plastic in marine environment: A critical mechanism review. *Chemosphere* **2023**, *330*, 138572.

[8] Sridhar, A.; Kannan, D.; Kapoor, A.; Prabhakar, S. Extraction and detection methods of microplastics in food and marine systems: A critical review. *Chemosphere* **2022**, *286*, 131653.

[9] Asamoah, B. O.; Uurasjärvi, E.; Räty, J.; Koistinen, A.; Roussey, M.; Peiponen, K. E. Towards the development of portable and *in situ* optical devices for detection of micro- and nanoplastics in water: A review on the current status. *Polymers* **2021**, *13*, 730.

[10] Sahai, H.; Aguilera del Real, A. M.; Alcayde, A.; Bueno, M. J. M.; Wang, C.; Hernando, M. D.; Fernández-Alba, A. R. Key insights into microplastic pollution in agricultural soils: A comprehensive review of worldwide trends, sources, distribution, characteristics and analytical approaches. *TrAC Trends Analy. Chem.* **2025**, *185*, 118176.

[11] Jin, M. Q.; Zhou, Q. W.; Fu, L.; Lin, C. T.; Wu, W. H. Microplastic contamination in sediments: Analytical techniques and case-based evaluations. *Talanta* **2025**, *294*, 128267.

[12] Samanta, P.; Dey, S.; Kundu, D.; Dutta, D.; Jambulkar, R.; Mishra,

R.; Ghosh, A. R.; Kumar, S. An insight on sampling, identification, quantification and characteristics of microplastics in solid wastes. *Trends Environ. Analy. Chem.* **2022**, *36*, e00181.

[13] Materić, D.; Kjær, H. A.; Vallelonga, P.; Tison, J. L.; Röckmann, T.; Holzinger, R. Nanoplastics measurements in Northern and Southern polar ice. *Environ. Res.* **2022**, *208*, 112741.

[14] Wang, Y. H.; Xu, X. Q.; Wu, J. Y.; Dong, Z. B.; Su, Y.; Huang, G. F.; Guo, Q.; Feng, Z. X.; Jia, H. Z.; Zhao, J. et al. Microplastics and nanoplastics on Mt. *Everest. Cell Rep. Sustain.* **2025**, *2*, 100467.

[15] Materić, D.; Ludewig, E.; Brunner, D.; Röckmann, T.; Holzinger, R. Nanoplastics transport to the remote, high-altitude Alps. *Environ. Pollut.* **2021**, *288*, 117697.

[16] Huang, P.; Cao, L. P.; Du, J. L.; Guo, Y. Q.; Li, Q. J.; Sun, Y.; Zhu, H. J.; Xu, G. C.; Gao, J. C. Polystyrene nanoplastics amplify the toxic effects of PFOA on the Chinese mitten crab (*Eriocheir sinensis*). *J. Hazard. Mater.* **2025**, *488*, 137488.

[17] Sun, N.; Hu, S. Y.; Zhao, X. C.; Gao, C. Z.; Liu, R. T. Amplification of benzo[*a*]pyrene toxicity persistence in earthworms by polystyrene nanoplastics: From organismal health to molecular responses. *J. Hazard. Mater.* **2025**, *487*, 137091.

[18] Qi, L. B.; Qin, W. Unveiling the fast adsorption and desorption of heavy metals on/off nanoplastics by real-time *in-situ* potentiometric sensing. *Sci. Total Environ.* **2024**, *943*, 173789.

[19] Li, H. Y.; Ding, Y. N.; Xu, Y.; Liu, W. Multi-omics insights into surface charge effects to decode the interplay of nanoplastics and bacterial antibiotic resistance. *iMeta* **2025**, *4*, e70056.

[20] Wang, Y. L.; Wang, Y. X.; Liu, M. H.; Jia, R. Q.; Zhang, Y.; Sun, G. J. W.; Zhang, Z. J.; Liu, M. J.; Jiang, Y. Micro-/nano-plastics as vectors of heavy metals and stress response of ciliates using transcriptomic and metabolomic analyses. *Environ. Pollut.* **2024**, *360*, 124667.

[21] Zhao, J.; Lan, R. Y.; Tan, H. M.; Wang, J. J.; Ma, Y. S.; Chen, Q. Q.; Jiang, F.; Wang, Z. Y.; Xing, B. S. Detection and characterization of microplastics and nanoplastics in biological samples. *Nat. Rev. Bioeng.* **2025**, *3*, 1019–1033.

[22] Sun, X. X.; Meng, L. J.; Liang, J. H.; Li, Q. J.; Du, J.; Zhu, M. L.; Zhao, Y. F.; Zheng, S. Microplastic distribution patterns in fish and implications for safe consumption. *Environ. Sci. Technol.* **2025**, *59*, 17393–17402.

[23] Rawat, H.; Gaur, A.; Singh, N.; Selvaraj, M.; Karnwal, A.; Pant, G.; Malik, T. Artificial intelligence-driven detection of microplastics in food: A comprehensive review of sources, health risks, detection techniques, and emerging artificial intelligence solutions. *Food Chem.: X* **2025**, *29*, 102687.

[24] Guo, X.; Lin, H.; Xu, S. P.; He, L. L. Recent advances in spectroscopic techniques for the analysis of microplastics in food. *J. Agric. Food Chem.* **2022**, *70*, 1410–1422.

[25] Zhao, J.; Lan, R. Y.; Wang, Z. Y.; Su, W. L.; Song, D. P.; Xue, R. Z.; Liu, Z. M.; Liu, X.; Dai, Y. H.; Yue, T. T. et al. Microplastic fragmentation by rotifers in aquatic ecosystems contributes to global nanoplastic pollution. *Nat. Nanotechnol* **2024**, *19*, 406–414.

[26] Yang, L. P.; Wang, W. X. Nanoplastics transport in zebrafish brain: Molecular and phenotypic behavioral impacts. *J. Hazard. Mater.* **2025**, *494*, 138548.

[27] Wang, M. J.; Li, Q. Q.; Shi, C. Z.; Lv, J.; Xu, Y. D.; Yang, J. J.; Chua, S. L.; Jia, L. R.; Chen, H. W.; Liu, Q. et al. Oligomer nanoparticle release from polylactic acid plastics catalysed by gut enzymes triggers acute inflammation. *Nat. Nanotechnol* **2023**, *18*, 403–411.

[28] Nihart, A. J.; Garcia, M. A.; El Hayek, E.; Liu, R.; Olewine, M.; Kingston, J. D.; Castillo, E. F.; Gullapalli, R. R.; Howard, T.; Bleske, B. et al. Bioaccumulation of microplastics in decedent human brains. *Nat. Med.* **2025**, *31*, 1114–1119.

[29] Lee, Y. H.; Zheng, C. M.; Wang, Y. J.; Wang, Y. L.; Chiu, H. W. Effects of microplastics and nanoplastics on the kidney and cardiovascular system. *Nat. Rev. Nephrol.* **2025**, *21*, 585–596.

[30] Lamoree, M. H.; van Boxel, J.; Nardella, F.; Houthuijs, K. J.; Brandsma, S. H.; Béen, F.; van Duursen, M. B. M. Health impacts of microplastic and nanoplastic exposure. *Nat. Med.* **2025**, *31*, 2873–2887.

[31] Huvet, A.; Le Gall, M.; Gilante, H.; Paul‐Pont, I. The issues of micro-nanoplastics in the oyster and mussel aquaculture sector. *Rev. Aquac.* **2025**, *17*, e70047.

[32] Rillig, M. C.; Kim, S. W.; Zhu, Y. G. The soil plastisphere. *Nat. Rev. Microbiol* **2024**, *22*, 64–74.

[33] Nava, V.; Dar, J. Y.; De Santis, V.; Fehlinger, L.; Pasqualini, J.; Adekolurejo, O. A.; Burri, B.; Cabrerizo, M. J.; Chonova, T.; Cour, M. et al. Zooming in the plastisphere: The ecological interface for phytoplankton–plastic interactions in aquatic ecosystems. *Biol. Rev.* **2025**, *100*, 834–854.

[34] Liu, X. W.; Xu, R. R.; Wu, H. Y.; Xu, K. W.; Zhang, W. J.; Wang, Z. Y.; Gong, W. W. Nanoplastics promote the dissemination of antibiotic resistance through conjugative gene transfer: Implications from oxidative stress and gene expression. *Environ. Sci.: Nano* **2023**, *10*, 1329–1340.

[35] Chen, L.; Lin, A. Q.; Tang, B. F.; Li, K. L.; Qian, Y.; Liu, X.; Zhang, Y. S.; Deng, Y. H.; Chen, W. T.; Zhao, Q. et al. The future of cancer therapy: Nanomaterials and tumor microenvironment. *iMetaMed* **2025**, *1*, e70007.

[36] Wen, J. K.; Lin, Y. H. Invisible invaders: Unveiling the carcinogenic threat of microplastics and nanoplastics in colorectal cancer—a systematic review. *Front. Public Health* **2025**, *13*, 1653245.

[37] Lin, A. Q.; Ye, P. X.; Li, Z. R.; Jiang, A. M.; Liu, Z. Q.; Cheng, Q.; Zhang, J.; Luo, P. Natural killer cell immune checkpoints and their therapeutic targeting in cancer treatment. *Research* **2025**, *8*, 0723.

[38] Lin, A. Q.; Xiong, M. Y.; Jiang, A. M.; Huang, L. H. Y.; Wong, H. Z. H.; Feng, S. Y.; Zhang, C. Y.; Li, Y.; Chen, L.; Chi, H. et al. The microbiome in cancer. *iMeta* **2025**, *4*, e70070.

[39] Aloia, R.; Annunziata, L.; Di Giacinto, F.; De Simone, S.; Profico, C.; Fanelli, I.; Di Francesco, G.; Mussi, V.; Scortichini, G. Application of Raman spectroscopy for the analysis of microplastics in food and beverages: A comprehensive review. *Appl. Spectrosc. Rev.*, in press, DOI: 10.1080/05704928.2025.2512771.

[40] Chakraborty, I.; Banik, S.; Biswas, R.; Yamamoto, T.; Noothalapati, H.; Mazumder, N. Raman spectroscopy for microplastic detection in water sources: A systematic review. *Int. J. Environ. Sci. Technol.* **2023**, *20*, 10435–10448.

[41] Chen, Q.; Wang, J. M.; Yao, F. Q.; Zhang, W.; Qi, X. H.; Gao, X.; Liu, Y.; Wang, J. M.; Zou, M. Q.; Liang, P. A review of recent progress in the application of Raman spectroscopy and SERS detection of microplastics and derivatives. *Microchim. Acta* **2023**, *190*, 465.

[42] Dai, H.; Li, H. Y.; Qiu, W.; Deng, S. Hai. ; Han, Jie.; Aminabhavi, Tejraj. Nondestructive analysis of plastic debris from micro to nano sizes: A state-of-the-art review on Raman spectroscopy-based techniques. *TrAC Trends Anal. Chem.* **2024**, *176*, 117750.

[43] Ly, N. H.; Kim, M. K.; Lee, H.; Lee, C.; Son, S. J.; Zoh, K. D.; Vasseghian, Y.; Joo, S. W. Advanced microplastic monitoring using Raman spectroscopy with a combination of nanostructure-based substrates. *J. Nanostruct. Chem.* **2022**, *12*, 865–888.

[44] Pei, W. Q.; Hu, R.; Liu, H.; Wang, L.; Lai, Y. C. Advanced Raman spectroscopy for nanoplastics analysis: Progress and perspective. *TrAC Trends Anal. Chem.* **2023**, *166*, 117188.

[45] Vasudeva, M.; Warrier, A. K.; Kartha, V. B.; Unnikrishnan, V. K. Advances in microplastic characterization: Spectroscopic techniques

and heavy metal adsorption insights. *TrAC Trends Anal. Chem.* **2025**, *183*, 118111.

[46] Xie, L. F.; Gong, K. D.; Liu, Y. Y.; Zhang, L. W. Strategies and challenges of identifying nanoplastics in environment by surface-enhanced Raman spectroscopy. *Environ. Sci. Technol.* **2023**, *57*, 25–43.

[47] Kutralam-Muniasamy, G.; Shruti, V. C.; Pérez-Guevara, F.; Flores, J. A. The emerging field of inductively coupled plasma mass spectrometry for (micro)nanoplastic analysis: "The 3As" analysis, advances, and applications. *TrAC Trends Anal. Chem.* **2024**, *174*, 117673.

[48] Fang, C.; Luo, Y. L.; Naidu, R. Microplastics and nanoplastics analysis: Options, imaging, advancements and challenges. *TrAC Trends Anal. Chem.* **2023**, *166*, 117158.

[49] Francischini, D. S.; Arruda, M. A. Z. When a picture is worth a thousand words: Molecular and elemental imaging applied to environmental analysis-A review. *Microchem. J.* **2021**, *169*, 106526.

[50] Huang, Z. K.; Hu, B.; Wang, H. Analytical methods for microplastics in the environment: A review. *Environ. Chem. Lett.* **2023**, *21*, 383–401.

[51] Jung, S.; Cho, S. H.; Kim, K. H.; Kwon, E. E. Progress in quantitative analysis of microplastics in the environment: A review. *Chem. Eng. J.* **2021**, *422*, 130154.

[52] Santos, F. A.; Andre, R. S.; Alvarenga, A. D.; Alves, A. L. M. M.; Correa, D. S. Micro- and nanoplastics in the environment: A comprehensive review on detection techniques. *Environ. Sci.: Nano* **2025**, *12*, 3442–3467.

[53] Shi, Y. Q.; Shi, L. P.; Huang, H. X. Y.; Ye, K. F.; Yang, L. M.; Wang, Z.; Sun, Y. F.; Li, D. Z.; Shi, Y. H.; Xiao, L. W. et al. Analysis of aged microplastics: A review. *Environ. Chem. Lett.* **2024**, *22*, 1861–1888.

[54] Xie, L. F.; Ma, M. L.; Ge, Q. Y.; Liu, Y. Y.; Zhang, L. W. Machine learning advancements and strategies in microplastic and nanoplastic detection. *Environ. Sci. Technol.* **2025**, *59*, 8885–8899.

[55] Srivastava, S.; Wang, W.; Zhou, W.; Jin, M.; Vikesland, P. J. Machine learning-assisted surface-enhanced Raman spectroscopy detection for environmental applications: A review. *Environ. Sci. Technol.* **2024**, *58*, 20830–20848.

[56] Pérez-Guevara, F.; Kutralam-Muniasamy, G.; Shruti, V. C. Critical review on microplastics in fecal matter: Research progress, analytical methods and future outlook. *Sci. Total Environ.* **2021**, *778*, 146395.

[57] Tan, M. Y.; Sun, Y.; Gui, J. X.; Wang, J. L.; Chen, X.; Wu, D. L. The efficiency of different digestion and separation methods for extracting microplastics in typical organic solid waste. *Int. J. Environ. Res.* **2022**, *16*, 16.

[58] Huang, K. Y.; Xie, L. Y.; Gu, X. Y.; Xie, J. Y.; Li, J. P.; Gao, S. X.; Ji, R.; Zhou, D. M. Comprehensive assessment of various digestion protocols for extraction microplastics from organic-rich environmental matrices. *Water Res.* **2025**, *282*, 123935.

[59] Liu, N. N.; Li, Z. F.; Cheng, S. K.; Monikh, F. A.; Ye, Z. W.; Ma, T. T.; Zheng, L.; Wang, X. M.; Ni, B. J.; Chen, Z. J. et al. Extracting and characterizing microplastics and nanoplastics from environmental samples. *Nat. Protoc.*, in press, DOI: 10.1038/s41596-025-01276-z.

[60] Nguyen, B.; Claveau-Mallet, D.; Hernandez, L. M.; Xu, E. G.; Farner, J. M.; Tufenkji, N. Separation and analysis of microplastics and nanoplastics in complex environmental samples. *Acc. Chem. Res.* **2019**, *52*, 858–866.

[61] Shi, X. F.; Mao, T. Y.; Huang, X. M.; Shi, H.; Jiang, K. Y.; Lan, R. Y.; Zhao, H.; Ma, J.; Zhao, J.; Xing, B. S. Capturing, enriching and detecting nanoplastics in water based on optical manipulation, surface-enhanced Raman scattering and microfluidics. *Nat. Water* **2025**, *3*, 449–460.

[62] Li, Q. C.; Lai, Y. J.; Yu, S. J.; Li, P.; Zhou, X. X.; Dong, L. J.; Liu, X.; Yao, Z. W.; Liu, J. F. Sequential isolation of microplastics and nanoplastics in environmental waters by membrane filtration, followed by cloud-point extraction. *Anal. Chem.* **2021**, *93*, 4559–4566.

[63] Xu, S. K.; Zhu, M. L.; Fan, L. H.; Yao, Y.; Cao, T. C.; Ji, R.; Hofmann, T.; Zhang, T.; Chen, W. Eco-corona formation enhances cotransport of nanoplastics and organic contaminants in porous media. *Environ. Sci. Technol.* **2025**, *59*, 12978–12989.

[64] Zhou, X. X.; He, S.; Gao, Y.; Li, Z. C.; Chi, H. Y.; Li, C. J.; Wang, D. J.; Yan, B. Protein corona-mediated extraction for quantitative analysis of nanoplastics in environmental waters by pyrolysis gas chromatography/mass spectrometry. *Anal. Chem.* **2021**, *93*, 6698–6705.

[65] Xu, Y. H.; Wang, X. T.; van der Hoek, J. P.; Liu, G.; Lompe, K. M. Natural organic matter stabilizes pristine nanoplastics but destabilizes photochemical weathered nanoplastics in monovalent electrolyte solutions. *Environ. Sci. Technol.* **2025**, *59*, 1822–1834.

[66] Liu, X.; Zhao, R. B.; Liu, M. H.; Zheng, T. Y.; Hao, Y. J.; Wang, C.; Liu, L.; Zhao, Y. T.; Liu, Z. M.; Dai, Y. H. et al. Transport of eco-corona coated nanoplastics in coastal sediments. *Water Res.* **2025**, *284*, 123893.

[67] Lane, T.; Wardani, I.; Koelmans, A. A. Exposure scenarios for human health risk assessment of nano- and microplastic particles. *Micropl. Nanopl.* **2025**, *5*, 28.

[68] Chen, Y. Q.; Shu, J. B.; Li, C. L.; Ye, X. N.; Li, Q.; George, C.; Chen, J. M. Size distribution of micro-/nanoplastic particles and their chemical speciation in the atmosphere of Shanghai, China. *Environ. Sci. Technol.* **2025**, *59*, 12833–12842.

[69] Gonçalves, J. M.; Bebianno, M. J. Nanoplastics impact on marine biota: A review. *Environ. Pollut.* **2021**, *273*, 116426.

[70] Ludescher, D.; Wesemann, L.; Schwab, J.; Karst, J.; Sulejman, S. B.; Ubl, M.; Clarke, B. O.; Roberts, A.; Giessen, H.; Hentschel, M. Optical sieve for nanoplastic detection, sizing and counting. *Nat. Photon.* **2025**, *19*, 1138–1145.

[71] Laborda, F.; Gimenez-Ingalaturre, A. C.; Bolea, E.; Castillo, J. R. Single particle inductively coupled plasma mass spectrometry as screening tool for detection of particles. *Spectrochim. Acta Part B: Atom. Spectrosc.* **2019**, *159*, 105654.

[72] Tang, J. J.; Eltaweil, A. S.; Adeyemi, A. S.; Jacobson, A. R.; Britt, D. W.; McLean, J. E.; Su, Y. M. Tracking the translocation of nanoplastics from soil to plant: Comparison of different analytical techniques. *J. Hazard. Mater.* **2025**, *488*, 137357.

[73] Jiménez-Lamana, J.; Marigliano, L.; Allouche, J.; Grassl, B.; Szpunar, J.; Reynaud, S. A novel strategy for the detection and quantification of nanoplastics by single particle inductively coupled plasma mass spectrometry (ICP-MS). *Anal. Chem.* **2020**, *92*, 11664–11672.

[74] Laborda, F.; Trujillo, C.; Lobinski, R. Analysis of microplastics in consumer products by single particle-inductively coupled plasma mass spectrometry using the carbon-13 isotope. *Talanta* **2021**, *221*, 121486.

[75] Liu, Z. Y.; Zhu, Y. J.; Lv, S. S.; Shi, Y. X.; Dong, S. F.; Yan, D.; Zhu, X. S.; Peng, R.; Keller, A. A.; Huang, Y. X. Quantifying the dynamics of polystyrene microplastics UV-aging process. *Environ. Sci. Technol. Lett.* **2021**, *9*, 50–56.

[76] Gonzalez de Vega, R.; Goyen, S.; Lockwood, T. E.; Doble, P. A.; Camp, E. F.; Clases, D. Characterisation of microplastics and unicellular algae in seawater by targeting carbon via single particle and single cell ICP-MS. *Anal. Chim. Acta* **2021**, *1174*, 338737.

[77] Hendriks, L.; Mitrano, D. M. Direct measurement of microplastics by carbon detection via single particle ICP-TOFMS in complex aqueous suspensions. *Environ. Sci. Technol.* **2023**, *57*, 7263–7272.

[78] Kong, F. F.; Fang, L.; Gui, Y. Y.; Lan, H. Y.; Zhao, P. P.; Zhang, Y. L.; Jiang, L. Y.; Zhang, S. Y.; Tong, X. M. Polyethylene and

polyvinyl chloride nanoplastics in human follicular fluid and seminal plasma: Impact on fertilization and sperm quality. *ACS Nano* **2025**, *19*, 27159–27172.

[79] Okoffo, E. D.; Thomas, K. V. Quantitative analysis of nanoplastics in environmental and potable waters by pyrolysis-gas chromatography-mass spectrometry. *J. Hazard. Mater.* **2024**, *464*, 133013.

[80] Ryzhenko, N.; Pecheul, G.; Dia, A.; Dutruch, L.; Pattier, M.; Pédrot, M.; Gigault, J.; Davranche, M. Bridging lab and field: Tracking environmentally relevant nanoplastics in crops using Py-GC/MS. *J. Hazard, Mater.* **2025**, *497*, 139693.

[81] Goedecke, C.; Eisentraut, P.; Altmann, K.; Elert, A. M.; Bannick, C. G.; Ricking, M.; Obermaier, N.; Barthel, A. K.; Schmitt, T.; Jekel, M. et al. Development of a routine screening method for the microplastic mass content in a wastewater treatment plant effluent. *Front. Environ. Chem.* **2022**, *3*, 844633.

[82] Sorolla-Rosario, D.; Llorca-Porcel, J.; Pérez-Martínez, M.; Lozano-Castelló, D.; Bueno-López, A. Microplastics' analysis in water: Easy handling of samples by a new thermal extraction desorption–gas chromatography-mass spectrometry (TED-GC/MS) methodology. *Talanta* **2023**, *253*, 123829.

[83] Wang, L.; Peng, Y. W.; Xu, Y. L.; Zhang, J. J.; Zhang, T.; Yan, M. Q.; Sun, H. W. An *in situ* depolymerization and liquid chromatography-tandem mass spectrometry method for quantifying polylactic acid microplastics in environmental samples. *Environ. Sci. Technol.* **2022**, *56*, 13029–13035.

[84] Chen, H.; Shan, X. L.; Qiu, X. R.; Ding, L.; Liang, X. J.; Guo, X. T. High-resolution mass spectrometry combined with reactive oxygen species reveals differences in photoreactivity of dissolved organic matter from microplastic sources in aqueous environments. *Environ. Sci. Technol.* **2024**, *58*, 10334–10346.

[85] Albergamo, V.; Wohlleben, W.; Plata, D. L. Tracking dynamic chemical reactivity networks with high-resolution mass spectrometry: A case of microplastic-derived dissolved organic carbon. *Environ. Sci. Technol.* **2024**, *58*, 4314–4325.

[86] Xiao, M. Y.; Yang, Y. Q.; Alahmadi, H.; Harbolic, A.; Moreno, G. M.; Yu, T.; Liu, J.; Guo, A.; Warner, G. R.; Stapleton, P. A. et al. Rapid detection of microplastics and nanoplastics in seconds by mass spectrometry. *J. Hazard. Mater.* **2025**, *493*, 138322.

[87] Erdogan, R. T.; Alkhaled, M.; Kaynak, B. E.; Alhmoud, H.; Pisheh, H. S.; Kelleci, M.; Karakurt, I.; Yanik, C.; Şen, Z. B.; Sari, B. et al. Atmospheric pressure mass spectrometry of single viruses and nanoparticles by nanoelectromechanical systems. *ACS Nano* **2022**, *16*, 3821–3833.

[88] Wu, Z. Y.; Janssen, S. E.; Tate, M. T.; Qin, M. H.; Wei, H. R. Regenerable membrane sensors for ultrasensitive nanoplastic quantification enabled by A data-driven Raman spectral processing algorithm. *Environ. Sci. Technol.* **2025**, *59*, 16652–16661.

[89] Liu, Y. S.; Zhan, Y. J.; Wang, G. F.; Jia, X. B.; Zhou, J.; Li, H. Q.; Chang, H. X.; Jin, Z. C.; Li, K.; Li, Z. X. Size-matching effects in quantitative detection of PS nanoplastics using controllable and reusable Ag nanoarrays SERS substrates. *J. Hazard. Mater.* **2025**, *494*, 138550.

[90] Zhang, J. J.; Peng, M.; Lian, E. K.; Xia, L.; Asimakopoulos, A. G.; Luo, S. H.; Wang, L. Identification of poly(ethylene terephthalate) nanoplastics in commercially bottled drinking water using surface-enhanced Raman spectroscopy. *Environ. Sci. Technol.* **2023**, *57*, 8365–8372.

[91] Lu, L. C.; Chen, W. R.; Kuo, C. L.; Wan, D. H. Portable surface-enhanced Raman scattering platform for rapid identification of nanoplastics at single-particle level. *J. Hazard. Mater.* **2025**, *498*, 139896.

[92] Xie, L. F.; Luo, S. H.; Liu, Y. Y.; Ruan, X. J.; Gong, K. D.; Ge, Q. Y.; Li, K. J.; Valev, V. K.; Liu, G. K.; Zhang, L. W. Automatic identification of individual nanoplastics by Raman spectroscopy based on machine learning. *Environ. Sci. Technol.* **2023**, *57*, 18203–18214.

[93] Ye, H. X.; Jiang, S. Y.; Yan, Y.; Zhao, B.; Grant, E. R.; Kitts, D. D.; Yada, R. Y.; Pratap-Singh, A.; Baldelli, A.; Yang, T. X. Integrating metal-phenolic networks-mediated separation and machine learning-aided surface-enhanced Raman spectroscopy for accurate nanoplastics quantification and classification. *ACS Nano* **2024**, *18*, 26281–26296.

[94] Guselnikova, O.; Trelin, A.; Kang, Y. Q.; Postnikov, P.; Kobashi, M.; Suzuki, A.; Shrestha, L. K.; Henzie, J.; Yamauchi, Y. Pretreatment-free SERS sensing of microplastics using a self-attention-based neural network on hierarchically porous Ag foams. *Nat. Commun.* **2024**, *15*, 4351.

[95] Wang, T.; Li, S.; Mu, R.; Lu, Z. W.; Su, J.; Chen, J.; Zhan, J. H. Size-resolved SERS detection of trace polystyrene nanoplastics via selective electrosorption. *Anal. Chem.* **2024**, *96*, 19545–19552.

[96] Gu, Y.; Li, Y. H.; Qiu, H. M.; Yang, Y. K.; Wu, Q. Y.; Fan, X. J.; Ding, Y. Y.; Yi, L. Z.; Ge, K.; Shen, Y. Z. Recent progress on noble-free substrates for surface-enhanced Raman spectroscopy analysis. *Coordin. Chem. Rev.* **2023**, *497*, 215425.

[97] Han, K. H.; Yan, Z. L.; Ding, Z.; Zhou, P. F.; Ye, C.; Qin, L.; Bao, Z. Y.; Zhang, M. F.; Zhang, W. High-sensitivity SERS sensor leveraging three-dimensional $Ti_3C_2T_x/TiO_2/W_{18}O_{49}$ semiconductor heterostructures for reliable detection of trace micro/nanoplastics in environmental matrices. *Talanta* **2025**, *286*, 127474.

[98] Dou, W. N.; Shao, M. R.; Ji, C.; Wu, Y.; Deng, S. Q.; Li, Z.; Yu, J.; Zhang, C.; Jiang, S. Z.; Zhao, X. F. et al. Investigation into the regulation of Ag NPs/ZnO NRs/GaN heterostructure SERS substrate via pyroelectric effects. *J. Phys. Chem. Lett.* **2025**, *16*, 9856–9863.

[99] Hu, M. Y.; Quan, Y. N.; Yang, S.; Su, R.; Liu, H. L.; Gao, M.; Chen, L.; Yang, J. H. Self-cleaning semiconductor heterojunction substrate: Ultrasensitive detection and photocatalytic degradation of organic pollutants for environmental remediation. *Microsyst. Nanoeng.* **2020**, *6*, 111.

[100] Kumar, K. M. A.; Kokulnathan, T.; Wang, T. J.; Weng, C. Y.; Chang, Y. H. Synergistic SERS enhancement of NiCo-LDHs microurchins and silver nanoparticles for ultra-sensitive and reusable detection of thiabendazole. *Sci. Total Environ.* **2024**, *950*, 175301.

[101] Mai, Q. D.; Thi Hanh Trang, D.; Thi Loan, N.; Tran Thi, N. H.; Van Hoang, O.; Ngoc Bach, T.; Quang Hoa, N.; Pham, A. T.; Le, A. T. Photo-induced-photo-catalytic SERS with silver-deposited TiO_2 nanorods for ultrasensitive and sustainable detection of low Raman cross-section molecules. *RSC Adv.* **2025**, *15*, 13172–13187.

[102] Ayeni, O.; Shondo, J. N.; Tjardts, T.; Şen, S.; Faupel, F.; Veziroglu, S.; Aktas, O. C.; Ameri, T. Photo-induced Raman amplification for detecting and monitoring degradation of micro- and nano-sized PVC plastics. *J. Mater. Chem. A* **2025**, *13*, 40886–40897.

[103] Mu, S.; Tian, Z. W.; Ren, W.; Liu, C. H. Laser-induced thermophoretic SERS enhancement on paper for facile pesticide and nanoplastic sensing. *Anal. Chem.* **2024**, *96*, 19840–19846.

[104] Moon, S.; Martin, L. M. A.; Kim, S.; Zhang, Q. S.; Zhang, R. Z.; Xu, W.; Luo, T. F. Direct observation and identification of nanoplastics in ocean water. *Sci. Adv.* **2024**, *10*, eadh1675.

[105] Yuan, Q.; Wang, Y. Q.; Mei, R. C.; Zhao, X. Z.; Song, J.; Chen, J. D.; Wu, Y. X.; Chen, L. X. Co-self-assembled monolayer enables sensitive SERS detection of nanoplastics via spontaneous hotspot entrapment. *Environ. Sci. Technol.* **2025**, *59*, 12292–12301.

[106] Yu, F. F.; Qu, C.; Ding, Z. X.; Wang, X.; Zheng, L. Q.; Su, M. K.; Liu, H. L. Liquid interfacial coassembly of plasmonic arrays and trace hydrophobic nanoplastics in edible oils for robust identification and classification by surface-enhanced Raman spectroscopy. *J. Agric. Food Chem.* **2023**, *71*, 14342–14350.

[107] Liu, Y.; Lin, L. Q.; Yang, B.; Huang, M. H.; Huang, X. X.; Chen, X.

X.; Dai, Z. Q.; Sun, S. L.; Yang, Y. Q.; Li, C. Y. Separation and identification of nanoplastics via a two-phase system combined with surface-enhanced Raman spectroscopy. *ACS Sustainable Chem. Eng.* **2024**, *12*, 1595–1604.

[108] Xing, F. Y.; Duan, W. M.; Tang, J. X.; Zhou, Y.; Guo, Z. J.; Zhang, H.; Xiong, J.; Fan, M. K. Superhydrophobic surface-enhanced Raman spectroscopy (SERS) substrates for sensitive detection of trace nanoplastics in water. *Anal. Chem.* **2025**, *97*, 2293–2299.

[109] Harris, R.; Berman, N.; Lampel, A. Coacervates as enzymatic microreactors. *Chem. Soc. Rev.* **2025**, *54*, 4183–4199.

[110] Ning, L. C.; Li, J. B.; Xie, Q. H.; Hu, J. N.; Liu, J.; Xu, C.; Peng, J. S.; Chen, C. X.; Ji, W. Plasmonic coacervate as a droplet-based SERS platform for rapid enrichment and microanalysis of hydrophobic payloads. *Anal. Chem.* **2024**, *96*, 18772–18780.

[111] Li, Y. M.; Wang, F.; Zhao, J.; Han, S.; Li, Y. T. DC versus AC electrokinetic-driven strategy coupled with a miniaturized electrochemical-SERS hydrogel chip toward dynamic monitoring of microplastics. *Anal. Chem.* **2025**, *97*, 20088–20096.

[112] Yu, E. S.; Jeong, E. T.; Lee, S.; Kim, I. S.; Chung, S.; Han, S.; Choi, I.; Ryu, Y. S. Real-time underwater nanoplastic detection beyond the diffusion limit and low Raman scattering cross-section via electro-photonic tweezers. *ACS Nano* **2023**, *17*, 2114–2123.

[113] Lê, Q. T.; Ly, N. H.; Kim, M. K.; Lim, S. H.; Son, S. J.; Zoh, K. D.; Joo, S. W. Nanostructured Raman substrates for the sensitive detection of submicrometer-sized plastic pollutants in water. *J. Hazard. Mater.* **2021**, *402*, 123499.

[114] Kim, W. H.; Lee, S.; Jeon, M. J.; Lee, K. J.; Park, J. H.; Park, D. W.; Park, S.; Sim, S. J. Rapid and differential diagnosis of sepsis stages using an advanced 3D plasmonic bimetallic alloy nanoarchitecture-based SERS biosensor combined with machine learning for multiple analyte identification. *Adv. Sci.* **2025**, *12*, 2414688.

[115] Seo, J.; Shin, G.; Shin, D. Metal-free AAO membranes function as both filters and Raman enhancers for the analysis of nanoplastics. *Water Res.* **2025**, *273*, 123043.

[116] Ruan, X. J.; Ao, J. P.; Ma, M. L.; Jones, R. R.; Liu, J.; Li, K. J.; Ge, Q. Y.; Xu, G. J.; Liu, Y. Y.; Wang, T. et al. Nanoplastics detected in commercial sea salt. *Environ. Sci. Technol.* **2024**, *58*, 9091–9101.

[117] Kim, S. J.; Ryu, G.; Chang, J.; Kim, D. G.; Park, Y. H.; Kim, Y. J.; Kim, S. Field-assisted efficient capturing and analysis of airborne nanoparticulate matter using a multifunctional nanoporous membrane. *ACS Appl. Mater. Interfaces* **2024**, *16*, 44261–44269.

[118] Jiang, Y.; Wang, X. C.; Zhao, G.; Shi, Y. Y.; Wu, Y.; Yang, H. L.; Zhao, F. Y. Silver nanostars arrayed on GO/MWCNT composite membranes for enrichment and SERS detection of polystyrene nanoplastics in water. *Water Res.* **2024**, *255*, 121444.

[119] Kim, J. Y.; Koh, E. H.; Yang, J. Y.; Mun, C.; Lee, S.; Lee, H.; Kim, J.; Park, S. G.; Kang, M.; Kim, D. H. et al. 3D plasmonic gold nanopocket structure for SERS machine learning-based microplastic detection. *Adv. Funct. Mater.* **2024**, *34*, 2307584.

[120] Yang, Q.; Zhang, S. Y.; Su, J.; Li, S.; Lv, X. C.; Chen, J.; Lai, Y. C.; Zhan, J. H. Identification of trace polystyrene nanoplastics down to 50 nm by the hyphenated method of filtration and surface-enhanced Raman spectroscopy based on silver nanowire membranes. *Environ. Sci. Technol.* **2022**, *56*, 10818–10828.

[121] Yang, Z. Y.; Zhu, K.; Yang, K.; Qing, Y.; Zhao, Y. J.; Wu, L.; Zong, S. F.; Cui, Y. P.; Wang, Z. Y. One-step detection of nanoplastics in aquatic environments using a portable SERS chessboard substrate. *Talanta* **2025**, *282*, 127076.

[122] Ardini, B.; Pittura, L.; Frontini, A.; Benedetti, M.; Gorbi, S.; Regoli, F.; Cerullo, G.; Valentini, G.; Manzoni, C. Fast detection and classification of microplastics by a wide-field fourier transform Raman microscope. *Environ. Sci. Technol.* **2025**, *59*, 9255–9264.

[123] Ardini, B.; Bassi, A.; Candeo, A.; Genco, A.; Trovatello, C.; Liu, F.; Zhu, X.; Valentini, G.; Cerullo, G.; Vanna, R. et al. High-throughput multimodal wide-field Fourier-transform Raman microscope. *Optica* **2023**, *10*, 663–670.

[124] Wu, Q. Y.; Xiao, D. Y.; Wang, N.; Masia, F.; Langbein, W.; Li, B. Rapid identification of micro and nanoplastics by line scan Raman micro-spectroscopy. *Talanta* **2024**, *266*, 125067.

[125] Rhee, H.; Jeong, S.; Lee, H.; Cho, M. G.; Choi, D. S. Rapid detection and identification of microplastics from nonchemically treated soil with CARS microspectroscopy. *Environ. Pollut.* **2024**, *342*, 123080.

[126] Kwak, J. I.; Rhee, H.; Kim, L.; An, Y. J. *In vivo* visualization of environmentally relevant microplastics and evaluation of gut barrier damages in *Artemia franciscana*. *J. Hazard. Mater.* **2024**, *478*, 135596.

[127] Zhang, Y. J.; Lu, M. J.; Wu, T.; Chen, K.; Feng, Y. X.; Wang, W. H.; Li, Y.; Wei, H. Y. Delay-spectral focusing dual-comb coherent Raman spectroscopy for rapid detection in the high-wavenumber region. *ACS Photonics* **2022**, *9*, 1385–1394.

[128] Takahashi, T.; Herdzik, K. P.; Bourdakos, K. N.; Read, J. A.; Mahajan, S. Selective imaging of microplastic and organic particles in flow by multimodal coherent anti-stokes Raman scattering and two-photon excited autofluorescence analysis. *Anal. Chem.* **2021**, *93*, 5234–5240.

[129] Choi, D. S.; Lim, S.; Park, J. S.; Kim, C. H.; Rhee, H.; Cho, M. Label-free live-cell imaging of internalized microplastics and cytoplasmic organelles with multicolor CARS microscopy. *Environ. Sci. Technol.* **2022**, *56*, 3045–3055.

[130] Ao, J. P.; Xu, G. J.; Wu, H.; Xie, L. F.; Liu, J.; Gong, K. D.; Ruan, X. J.; Han, J.; Li, K. J.; Wang, W. et al. Fast detection and 3D imaging of nanoplastics and microplastics by stimulated Raman scattering microscopy. *Cell Rep. Phys. Sci.* **2023**, *4*, 101623.

[131] Qian, N. X.; Gao, X.; Lang, X. Q.; Deng, H. P.; Bratu, T. M.; Chen, Q. X.; Stapleton, P.; Yan, B. Z.; Min, W. Rapid single-particle chemical imaging of nanoplastics by SRS microscopy. *Proc. Natl. Acad. Sci. USA* **2024**, *121*, e2300582121.

[132] Huber, M. J.; Zada, L.; Ivleva, N. P.; Ariese, F. Multi-parameter analysis of nanoplastics in flow: Taking advantage of high sensitivity and time resolution enabled by stimulated Raman scattering. *Anal. Chem.* **2024**, *96*, 8949–8955.

[133] Wang, M.; Huang, Z. L.; Wu, C.; Yan, S.; Fang, H. T.; Pan, W.; Tan, Q. G.; Pan, K.; Ji, R.; Yang, L. Y. et al. Stimulated Raman scattering microscopy reveals bioaccumulation of small microplastics in protozoa from natural waters. *Environ. Sci. Technol.* **2024**, *58*, 2922–2930.

[134] Xin, L.; Huang, M. Z.; Huang, Z. W. Quantitative assessment and monitoring of microplastics and nanoplastics distributions and lipid metabolism in live zebrafish using hyperspectral stimulated Raman scattering microscopy. *Environ. Int.* **2024**, *187*, 108679.

[135] Galluzzi, M.; Lancia, M.; Zheng, C.; Re, V.; Castelvetro, V.; Guo, S. F.; Viaroli, S. Atomic force microscopy (AFM) nanomechanical characterization of micro- and nanoplastics to support environmental investigations in groundwater. *Emerg. Contam.* **2025**, *11*, 100478.

[136] Chen, X. Q.; Huang, W. Y.; Tang, Y.; Zhang, R. Z.; Lu, X. Y.; Liu, Y.; Zhu, M. D.; Fan, X. Y. Variation of Young's modulus suggested the main active sites for four different aging plastics at an early age time. *J. Hazard. Mater.* **2024**, *470*, 134189.

[137] Huang, W. Y.; Jiang, G. Q.; Xie, L. D.; Chen, X. Q.; Zhang, R. Z.; Fan, X. Y. Effect of oxygen-containing functional groups on the micromechanical behavior of biodegradable plastics and their formation of microplastics during aging. *J. Hazard. Mater.* **2024**, *463*, 132911.

[138] Li, D. Z.; Li, P. J.; Shi, Y. H.; Sheerin, E. D.; Zhang, Z. H.; Yang, L. M.; Xiao, L. W.; Hill, C.; Gordon, C.; Ruether, M. et al. Stress-induced phase separation in plastics drives the release of amorphous polymer micropollutants into water. *Nat. Commun.* **2025**, *16*, 3814.

[139] Belontz, S. L.; Brahney, J.; Caplan, C. E.; Dillon, E.; Yan, T.;

Dominguez, G. Combining submicron spectroscopy techniques (AFM-IR and O-PTIR) to detect and quantify microplastics and nanoplastics in snow from a Utah ski resort. *Environ. Sci. Technol.* **2025**, *59*, 13362–13373.

[140] Li, Y.; Zhang, C. M.; Tian, Z. Y.; Cai, X. Y.; Guan, B. H. Identification and quantification of nanoplastics (20–1000 nm) in a drinking water treatment plant using AFM–IR and Pyr-GC/MS. *J. Hazard. Mater.* **2024**, *463*, 132933.

[141] Xie, D. D.; Fang, H. Y.; Zhao, X.; Lin, Y.; Su, Z. H. Identification of microplastics and nanoplastics in environmental water by AFM–IR. *Anal. Chim. Acta* **2025**, *1354*, 343992.

[142] Luo, H. W.; Xiang, Y. H.; Li, Y.; Zhao, Y. Y.; Pan, X. L. Photocatalytic aging process of nano-TiO_2 coated polypropylene microplastics: Combining atomic force microscopy and infrared spectroscopy (AFM–IR) for nanoscale chemical characterization. *J. Hazard. Mater.* **2021**, *404*, 124159.

[143] Zhang, W.; Dong, Z. Q.; Zhu, L.; Hou, Y. Z.; Qiu, Y. P. Direct observation of the release of nanoplastics from commercially recycled plastics with correlative Raman imaging and scanning electron microscopy. *ACS Nano* **2020**, *14*, 7920–7926.

[144] Li, G.; Yang, Z. R.; Pei, Z. G.; Li, Y. M.; Yang, R. Q.; Liang, Y.; Zhang, Q. H.; Jiang, G. B. Single-particle analysis of micro/nanoplastics by SEM-Raman technique. *Talanta* **2022**, *249*, 123701.

[145] Böke, J. S.; Popp, J.; Krafft, C. Optical photothermal infrared spectroscopy with simultaneously acquired Raman spectroscopy for two-dimensional microplastic identification. *Sci. Rep.* **2022**, *12*, 18785.

[146] Parham, R. L.; Ayala, A. M.; Meagher, L.; Clough, M. E.; Ochoa Rivera, E.; Shi, J. H.; Tewari, A.; McNeil, A. J.; Ault, A. P. Identifying microplastics in laboratory and atmospheric aerosol mixtures via optical photothermal infrared and Raman microspectroscopy. *Anal. Chem.* **2025**, *97*, 18136–18143.